



TECHNISCHE
UNIVERSITÄT
WIEN
Vienna University of Technology

DIPLOMARBEIT

**Predicting Land Surface Temperatures in Urban Areas from
Landsat 8 Images – A GIS-Based Approach**

**ausgeführt zum Zwecke der Erlangung des akademischen Grades einer
Diplom-Ingenieurin**

unter der Leitung von

Univ.-Prof. DI Dr. Ardeshir Mahdavi

E 259-3 Abteilung für Bauphysik und Bauökologie

Institut für Architekturwissenschaften

eingereicht an der

Technischen Universität Wien

Fakultät für Architektur und Raumplanung

von

Caroline Walder

Matrikelnr. 11802565

Farberweg 17, 6380 St. Johann in Tirol

Wien, Februar 2021

KURZFASSUNG

Die vorliegende Forschungsarbeit untersucht den Einfluss flächennutzungsbezogener Änderungen auf das städtische Mikroklima der Stadt Wien (Österreich).

Auf Grundlage von Satellitenbildern sollen mit Hilfe von Geografischen Informationssystemen (GIS) klassifizierte Karten erstellt werden, womit Berechnungen zur Ermittlung der Oberflächentemperaturen zweier Referenzjahre durchgeführt werden können. Die errechneten Oberflächentemperaturen werden anschließend mit Hilfe eines statistischen Modells in die Zukunft projiziert, sodass Rückschlüsse auf einen möglichen Zusammenhang mit der Verstädterung gezogen werden können.

Die zur Erstellung der Karten herangezogenen Rasterdaten wurden vom Satelliten Landsat 8 bei ähnlichen Wetterbedingungen in den Jahren 2013 und 2020 aufgenommen.

Für die vorliegende Studie wurden die folgenden Hauptschritte unternommen:

- i) Literaturrecherche über den städtischen Hitzeinsel-Effekt ("Urban Heat Island Effect")
- ii) Erstellung der klassifizierten Flächenkarten mit den Klassen Wasser, bebaute Fläche, Grünfläche und Ackerland;
- iii) Projektion der Klassifizierung in die Zukunft;
- iv) Berechnung der Referenz-Oberflächentemperaturen mit Hilfe des Mono-Window-Algorithmus;
- v) Errechnung der künftigen Oberflächentemperaturen;
- vi) Statistische Analyse und Ableitung von Unterscheidungsmustern der Oberflächentemperaturen.

Die Analyse der Satellitenbilder unterstreicht den fortschreitenden Temperaturanstieg der Stadt Wien mit der Zeit im Vergleich zu den Ergebnissen der Ausgangsszenarien. Es ist eine Beziehung zwischen der zunehmenden Versiegelung städtischer Flächen und den ansteigenden Oberflächentemperaturen zu erkennen. Dieser Temperaturanstieg trägt zum Urban Heat Island Effect bei.

Im weiteren Verlauf der Forschungsarbeit werden Maßnahmen und Empfehlungen zur Eindämmung des Urban Heat Island Effect vorgestellt und bewertet.

Schlüsselbegriffe

Satellitendaten, Fernerkundung, Mikroklima, städtische Hitzeinsel, GIS

ABSTRACT

In this paper, geographic information system (GIS) techniques and satellite data are used in order to analyse the impact of changes in land use and land cover in the city of Vienna, Austria, on the local microclimate. Engaging satellite imagery, the city of Vienna was classified into four zones which allow for the calculation of land surface temperature in two reference years in the past. The classified maps were then statistically projected into the future, resulting in predicted land surface temperatures at a given point in the future. These findings highlight the relationship between urbanization and temperature rise in the urban context.

Both scenarios were processed with data downloaded from Landsat 8 satellite in 2013 and 2020, at similar weather conditions.

The main stages of the study are:

- i) Review of the current literature regarding urban heat island effect;
- ii) Generation of land cover maps for past and present conditions;
- iii) Projection of the land cover maps into the future;
- iv) Calculation of past and present scenario land surface temperatures using Mono-Window algorithm;
- v) Statistical projection of predicted land surface temperatures with a linear regression model;
- vi) Derivation of land surface temperature difference patterns.

The analysis of satellite data highlights higher values of the land surface temperatures in the city of Vienna at later stages in time compared to the past condition scenario of 2013. The statistical projection results stress the increase in land surface temperature in the urban context. The reason for the rising land surface temperatures are correlating with change in land use and land cover caused by urbanization.

Lastly, the study provides and evaluates urban heat island effect mitigation measures.

Keywords

Satellite data, remote sensing, microclimate, urban heat island effect, GIS

ACKNOWLEDGEMENTS

As part of finishing my master's program of Building Science and Technology at the TU Vienna, I would like to express my sincere gratitude to those who helped me during this period.

First of all, I would like to thank my supervisors from TU Vienna, Univ.-Prof. DI Dr. Ardeshir Mahdavi and Ms Pelin Firat Örs, for their guidance throughout the research project.

Likewise, I would like to thank my colleagues from Arup for supporting me with valuable sources of knowledge. My special thanks go to Jake Haskell for his encouragement and for challenging me to think outside the box.

Finally, I would like to express my deep gratitude to the people dearest to me. I would like to thank my beloved family for their unconditional support and love. This would not have been possible without you.

Thank you for being part of this journey. I hope that you will enjoy reading the current research.

CONTENTS

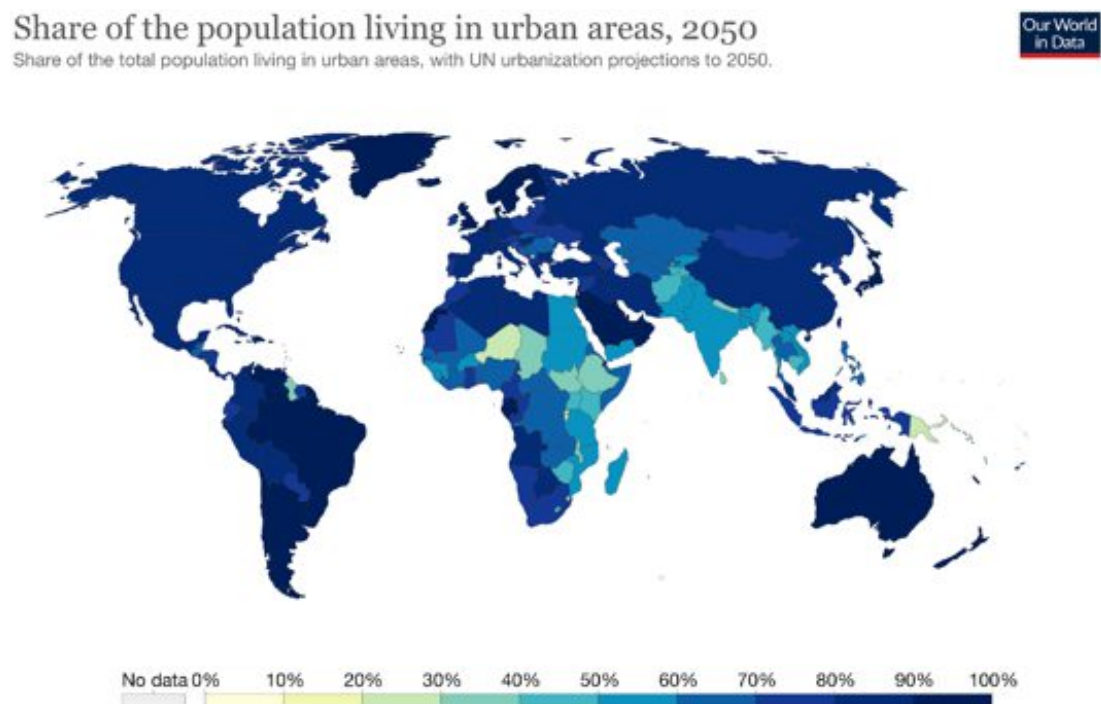
1	Introduction	1
1.1	Overview.....	1
1.2	Motivation	2
1.3	Background.....	2
1.4	Aim of the study	3
2	Literature Review	4
2.1	Urbanization.....	4
2.2	Land surface modification.....	5
2.3	Urban fabric	6
2.3.1	Radiative properties.....	6
2.3.2	Thermal properties.....	8
2.3.3	Environmental influencing factors.....	9
2.4	Urban morphology	12
3	Materials and Methods.....	14
3.1	Overview.....	14
3.1.1	Study site	14
3.1.2	Data acquisition	15
3.2	Land use/land cover classification.....	20
3.3	Land use/land cover prediction.....	24
3.4	Land surface temperature calculation	25
3.5	Land surface temperature projection.....	32
3.6	Hypothesis	32
4	Results	33
4.1	Post-processing.....	33
4.2	Land use/land cover	34
4.3	Land surface temperature	37
5	Conclusion	40
5.1	Results evaluation	40
5.2	Statistical validation	40
5.3	USGS Landsat Collection 2 Temperature Product.....	42
5.4	Limitations.....	45
5.4.1	Data basis.....	45
5.4.2	MOLUSCE.....	45
5.4.3	Image quality	46
5.5	Mitigation measures.....	47
5.5.1	Political strategies.....	47

5.5.2	Sustainable city development	48
5.5.3	Challenges	50
6	Discussion	51
7	Index	52
7.1	List of abbreviations	52
7.2	List of figures	54
7.3	List of tables	56
7.4	List of equations	57
8	Literature	58
9	Appendix	64

1 INTRODUCTION

1.1 Overview

Throughout the ongoing expansion and growth of urban areas and a current percentage of over 50 % of the world's population living in urban areas (Figure 1), the environment is expected to experience massive changes in the future. Due to this rapid increase of urbanization cities are forced to use and therefore seal surfaces in order to provide enough space for their occupants (Ritchie 2018).



Source: OWID based on UN World Urbanization Prospects 2018 and historical sources (see Sources/DurWorldInData.org/urbanization • CC BY
Note: Urban areas are defined based on national definitions which can vary by country.

Figure 1: Share of the world population living in urban areas, 2050 (Global Change Data Lab 2020)

The effects of removing natural surfaces from an urban site and replacing them with dense materials with high heat storage capacity like asphalt and concrete contribute to increasing air and surface temperatures. Thus, numerous cities already show higher air and surface temperatures than their rural surrounding areas, which is commonly known as the urban heat island (UHI) effect. As a result, UHI effect leads to a higher cooling demand in buildings during summertime, which contributes to an increase in energy consumption and greenhouse gas emissions. Moreover, the rise of intra-urban temperatures has a strong effect on the quality of life for humans, animals and on vegetation in general (Yang et al. 2016).

In this work, a conceptual framework for the prediction of land surface temperatures by analyzing satellite data in geographical information systems (GIS) is presented. GIS is a collection of computer software and information that can be used in order to display, analyze, generate and manage geographical data (QGIS 2016).

The methodology is applied to the city of Vienna, Austria, using satellite data collected by Landsat 8, provided by the United States Geological Survey (USGS). The research shall provide an overview of the driving forces of UHI effect as well as the recommended mitigation measures in order to approach sustainable development in urban areas.

This framework may be used as a GIS-related base for forecasting land surface temperature changes in urban sites due to land use and land cover change, and may contribute to a better understanding of UHI effect at an early stage in planning, master planning, expansion or densification of the urban space.

1.2 Motivation

The “Fridays for Future” movement achieved what only few previous strike demonstrations were able to: It drew the world’s attention on global climate change. Students across the world are skipping school on Fridays to fight for greater political action on climate change. The protesters argue that governments everywhere are globally failing to adopt policies ambitious enough to avoid the worst effects of climate change (Fridays For Future 2020).

According to the Intergovernmental Panel on Climate Change (IPCC), world emissions would have to be cut by 45 % by less than ten years, in order to stay below the 1.5 K global warming and to avoid a climate catastrophe which is considered to have terrific impacts on the world’s ecosystem, population and vegetation (IPCC 2018)

People living in cities have already been experiencing extraordinarily high peak temperature events over the last summers during daytime, compared to the previous century. But not only daytime temperatures have been rising dramatically; it could be obtained that the temperature level was hardly able to fall below 20 °C during nighttime (European Commission 2020).

1.3 Background

The investigation of land use/land cover and quantifying its changes with regard to land surface temperature is of growing importance in urban development. It is

generally understood that intra-urban temperatures are factors closely related to the quality of life of the majority of the population. Urbanization and new building construction methods dramatically affect UHI effect as well as air quality, and can deteriorate comfort for the occupants in the respective region (Favretto 2018).

One way of assessing the effects of urbanization is via land surface temperature (LST), which is the temperature of the ground surface, and is commonly used for environmental and climate change studies. Increasing surface temperature is one of the main effects of urbanization and driving forces of UHI: LST is rising due to anthropogenic heat discharges caused by energy consumption of high heat capacities and conductivities of artificial materials. Simultaneously, decreasing vegetation and therefore less permeability of surfaces through evapotranspiration are also contributing to temperature increase. Moreover, the rising temperatures affect comfort and forces people to install air conditioning and additional ventilation units in their homes in order to keep the indoor air temperature at a lower level (Sundara Kumar et al. 2012)

1.4 Aim of the study

The aim of the thesis is to present an overview of the driving forces and effects of UHI effect.

By projecting the land surface temperature in an urban setting from two scenarios into the future, the study shall allow for a better understanding of the relationship between urbanization and UHI effect.

Engaging the capital city of Austria, Vienna, as an example, the study shall present a GIS-based approach, starting from the data acquisition of satellite images to a statistical analysis in order to predict future land surface temperature scenarios.

Finally, the results shall be presented in a clear way and mitigation challenges shall be pointed out.

2 LITERATURE REVIEW

Urban heat island (UHI) effect is a type of heat accumulation phenomenon, in which heat is captured in urban areas due to their constructive conditions and actions executed by human beings. With the origin in the early 1800s, UHI effect was firstly investigated and interpreted by Luke Howard, a scholar from England. Howard recognized that the city center of London showed remarkably higher temperatures than the surrounding rural areas of the city. Howard initiated the perpetuating research of UHI effect globally. The ongoing studies concluded close dependencies between UHI effect and urban heat release, properties and structure of the respective underlying surfaces, vegetation, as well as demographic (i.e. population density) and climatic conditions (Yang et al. 2016).

Urban heat island effect is represented as a function of the intensity difference between zone temperatures according to the degree of urbanization. Equation (1) provides the mathematical definition of UHI effect.

$$UHI = \Delta T_{Z_u-r} \quad (1)$$

UHI is the intensity of the urban heat island effect, ΔT is the temperature difference between the zone with more urban components (Z_u) and the zone with less urban components (Z_r) (Stewart et al. 2012).

The existing literature was critically reviewed with an aim to investigate the concept of UHI effect in general and more specifically in correlation with the concept of sustainability and resilience at city scale. The review was also deployed to further investigate causes, effects and mitigation strategies of UHI effect.

2.1 Urbanization

The importance of studying UHI effect is growing on the one hand due to demographic change: Projections by the United Nations claim that 60 % or more of the world's population will be living in cities by 2025, even close to 70 % by 2050. With the steady growth of urban areas, their influences on "local, regional, and perhaps even the global" environment also keep increasing (Estes Jr. 2007).

Due to "urban sprawl", a phenomenon in which cities are simultaneously increasing in size and width, the number of heat waves in the cities is growing. As a result, this leads to more frequent extreme heat events. The fast-growing numbers in population living in urban areas will also contribute to not only warming of cities but also on the global scale. Moreover, it is anticipated that a loss of biodiversity and deforestation in

order to provide enough space to occupy people migrating from rural areas into the city will occur. As a consequence of the urban environment growth, vegetation will be driven out, unleashing an energy cost explosion, biophysical environmental collapses and affect human as well as natural ecosystems (Mohamed et al. 2017).

However, when defining urban areas, opinions differ widely. The countries adopt different definitions for what shall be considered an “urban area”, taking into account minimum population thresholds, population density, infrastructure development, employment type. In Austria, an urban area is typically defined by its population: the threshold value for a setting to be considered a “city” is 10,000 inhabitants (Mohr 2020).

2.2 Land surface modification

As stated in 2.1, urban areas need to be modified regarding space and spatial distribution in order to occupy the growing city population. This anticipates a change in the land surface, using more manmade materials and therefore forcibly reducing naturally vegetated surfaces such as bare soil, water bodies, forests etc. Surfaces typical for urban landscapes such as asphalt, cobblestone, roof claddings and other factitious materials absorb solar radiation during daytime and store it as heat energy due to higher heat storage capacity and lower albedo. Regarding their hydraulic, radiative and thermal properties, these materials significantly differ from their predecessor materials such as soil, rock, grass, and water. These engineered materials alter the surface and atmospheric circumstances, resulting in different energy, water and airflow conditions. Additionally, city density and anthropogenic exhaust energy from vehicles increasing air pollution result in deteriorating urban climatic conditions (Mohamed et al. 2017).

This development as well as land use and land cover (LULC) changes have a direct impact on land surface temperature (LST). Thus, LULC change leads to the replacement of soil and vegetated surfaces by water impermeable materials, agricultural operations, construction for the use of commercialism and industry, often situated in high-rise structures. So-called “grey structures” alter the urban biophysical climate and, as a consequence, affect LST. Subsequently, many studies drew parallels between the presence of green (vegetated or grass covered terrain) or blue (water bodies) urban surfaces, and reduced land surface temperatures and air temperatures in the respective area: the phenomenon of the “urban cooling island” (Yu et al. 2019).

As an example, analyses of the impact of urbanization on LST in the city of Taipei concluded that the diurnal variations (i.e. temperature differences between day- and nighttime) positively correlated with the remote sensing-based urbanization index (UI). Additionally, it was concluded that negative impacts were more likely to be discovered at an earlier stage of urbanization. (Chen et al. 2017)

Rapid transformation from e.g. natural land covers to impervious surfaces result in significant differences in local climatic conditions such as changes in LST and air temperature. Land surface and air temperature are among the key priority physical contributors affected by LULC changes (Khan et al. 2020).

2.3 Urban fabric

In general, the current choice of material used majorly roots in the construction industry. It led to the destruction of the urban thermal environment and the increase of energy use over the past decades. Nowadays high-performance buildings are designed to have appropriate material selection in terms of embodied energy level and CO₂ emissions. Furthermore, three main factors are playing the major role in the life cycle and performance of a building: building envelope, building type and technical building equipment. These three aspects, subsequently, affect energy expenditures of a building and contribute to UHI effect – directly (from the building envelope) as well as indirectly (e.g. embedded CO₂ emissions and operational energy for – as well as warm air emissions from – air conditioning) (Wonorahardjo et al. 2020).

The following paragraphs shall provide an insight into the physical influencing factors of air temperatures and surface temperatures in the urban context, in dependence of materials and their respective properties. For the purpose of simplifying the study, the following points will be neglected in the case study, but may be considered potential drivers of the results for future research.

According to the United States Environmental Protection Agency (US EPA), major driving factors of the UHI can be categorized into radiative and thermal properties as following (EPA 2017).

2.3.1 Radiative properties

Albedo

According to the Office of Energy Efficiency and Renewable Energy (EERE), solar radiation, also referred to as solar resource, is electromagnetic radiation emitted by the sun and can be transformed into e.g. heat and electricity. The amount of incident

solar radiation depends on the geographic location, date and time, topography and the weather (e.g. precipitation, cloud coverage) of the Earth's respective region. Due to characteristics of the Earth's atmosphere, solar radiation can be naturally reduced, which is called diffuse solar radiation. Diffusing factors can be air molecules, clouds, pollutants, forest fires or volcanoes (EERE 2013).

Albedo (al , [%]) is referred to as the reflectivity of an object's surface in space, the amount of electromagnetic radiation (i.e. solar radiation), that is being reflected away from the object due to its surface properties. A surface reflecting 100 % of the incident solar radiation would have an albedo of 1, whereas commonly known "black body", being completely dark and not capable of reflecting any electromagnetic radiation, would have an albedo of 0. In terms of this example, albedo has a crucial effect on the Earth, resulting in rising surface temperatures with more solar radiation absorbed due to lower albedo. Apart from that, clouds are able to reflect sunlight as well as to trap heat, warming up the planet. At any given moment, about 50 % of the world is covered with clouds, which makes taking them into account in measurements inevitable. The average albedo of the Earth is 0.367, whereas fresh snow and the ocean have an albedo of about 0.9 and 0.06, respectively. Land area surfaces range from 0.1 to 0.4 (Cain 2009).

Studies show that in the urban area building context a change in albedo has a respectively high potential to directly influence UHI effect. As an example, a recent study carried out in Brazil shows that the UHI intensity between two roof types with albedo 0.08 (e.g. asphalt) and 0.90 (e.g. white painting), respectively, can result in a temperature difference of 1.4 K. Moreover, the same study found that the reduction of the roof albedo to 0.08 increases the overall UHI intensity to an average of 0.2 K, while the cool roof (albedo 0.9) leads to a temperature decrease of 1 K for the whole study area. Eventually, the study finds that the more solar radiation reflected by the roof areas, less radiation is absorbed by the surface, which decreases the temperature and the UHI intensity (Bueno de Morias et al. 2019).

Emissivity

Based upon albedo, emissivity (ϵ , [%]) is the ratio of the energy radiated from an object's surface to the energy radiated from the "black body", the perfect emitter, referring to the same temperature and wavelength as well as viewing conditions. With an emissivity of 1, representing the black body, studies found a decrease in UHI intensity values of about 0.5 K on average. It was found that the differences in temperature are related to wind advection, where wind is carried from rural areas into

urban areas. Hence, using materials with close to black body properties contributes to this heat transport (Bueno de Morias et al. 2019).

Table 1 provides typical values for albedo (Kotak et al. 2015) and emissivity (Mohamed et al. 2017) values for surfaces to be found frequently in urban areas.

Table 1: Typical albedo (Kotak et al. 2015) and emissivity (Mohamed et al. 2017) values for different surface types

Surface	Albedo [%]	Emissivity [%]
Trees	0.15 – 0.18	0.96 – 0.99
Asphalt	0.05 – 0.2	0.90
Concrete	0.25 – 0.7	0.95
Grass	0.25 – 0.3	0.98 – 0.99
Ice	0.3 – 0.5	0.98
Water	0.5 – 0.7	0.99

2.3.2 Thermal properties

Heat capacity

Heat capacity (c , [J/K]) is a material's ability to store heat. Building materials like steel have higher heat capacities than natural materials such as soil or sand. Heat capacity is able to directly affect surface temperatures and, as a result, the surface-air interface. This contributes to a higher heat storage potential in urban areas than in rural areas. As an example, during daytime inner-city areas are capable of absorbing 200 % of the heat compared to their rural surrounding areas. The reason for this drastic difference is the type of materials to be found in urban areas such as pavement, asphalt, concrete, cobblestone. In contrast to that, rural areas are mostly covered by materials with low heat capacity, e.g. cropland, forests, etc. (Christen et al. 2004).

Studies found that a heat capacity increased by ten times leads to an UHI intensity reduction of 3.5 K and show that the differences starts at the point when the streets are exposed to solar radiation, indicating that the traffic areas (mostly asphalt) have a significantly contribute in transferring heat into the urban atmosphere. Moreover, the aspect-ratio affects temperature due to urban canyon effect, where more radiation is retained by taller buildings and narrow streets (Bueno de Morias et al. 2019).

Thermal conductivity

Thermal conductivity (λ , [W/m.K]) describes a material's ability to transfer heat. Not only does it affect the respective material's temperature but also the interface between surface and air, similar to heat capacity. According to Bueno de Morias et al. (2019), a decrease of thermal conductivity (and constant internal building loads) should result in reduced surface temperatures: By reducing thermal conductivity to 10 %, UHI intensity achieves temperature differences of up to 2 K lower than the original control values.

What is more, aspect-ratio plays a crucial role in assessing thermal conductivity, as the adjacent urban area decreased the temperature more than the city center. Due to the high rate of urban canyons, more radiation is absorbed in the city center, which, by implication, denotes a higher UHI intensity difference in the adjacent city region (Bueno de Morias et al. 2019).

Table 2 provides an overview of heat capacity and thermal conductivity values of materials to be found typically in an urban environment.

Table 2: Heat capacity and thermal conductivity values for different materials (Greenspec 2021)

Surface	Heat capacity [J/kg.K]	Thermal conductivity [W/m.K]
Water	4200	0.69
Stone	1000	1.8
Brick	800	0.73
Concrete	1000	1.13
Gypsum plaster	1000	0.5
Timber	1200	0.14
Steel	480	45

2.3.3 Environmental influencing factors

Vegetation

According to the National Aeronautics and Space Administration (NASA), the amount of vegetation present or absent in a space is essential for urban heating. Impervious surfaces, such as concrete, asphalt etc., mostly used in urban areas, absorb more

sunlight due to their physical properties than surrounding vegetated areas such as trees and grass. This is majorly happening during daytime when solar radiation is the strongest. Vegetated areas naturally cool the ambient air as a side effect during photosynthesis: Water is being released back into the atmosphere (i.e. evapotranspiration), naturally decreasing surface temperatures. The larger the pores on leaves, the more water can be exchanged and, consequently, the stronger is the cooling effect (Figure 2).

What is more, plants such as bushes or trees can provide shade to the neighboring buildings and surfaces which may be 11 °C to 25 °C cooler than the peak temperatures of unshaded materials (EPA 2008).

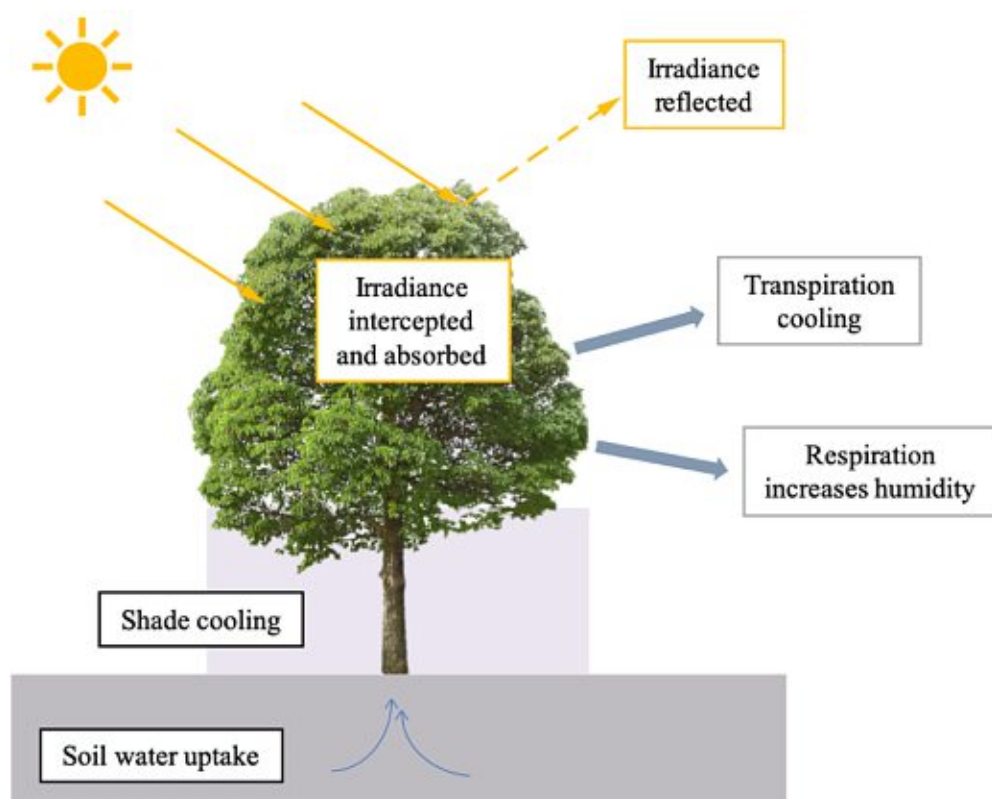


Figure 2: Natural cooling effect of a tree

It has been found, that a vegetation cover increased by 50 % in urbanized zones (study area: Querétaro, Mexico) would be able to lower UHI intensity up to 2.05 K during the warmest period (Colunga et al. 2015).

The Normalized Difference Vegetation Index (NDVI) and the Urbanization Index (UI) were found to be those factors to influence UHI the strongest. NDVI is a simple indicator of vegetated areas and biomass; UI is an indicator for built areas. The corresponding study showed that an increase in NDVI (from 80 % to 100 %) – and therefore more vegetated surfaces and trees – significantly decreased UHI intensity or even resulted in Urban Cool Island effect. What is more, the study showed that

areas with little to no greening only showed slight decrease in UHI intensity, resulting in close to zero change even if the small amount of vegetated areas had an NDVI of 100 % (Alves et al. 2017).

Weather

By taking a moment and thinking about the weather on a specific day, one can quickly identify if it is what would be expected or what would be typical for the respective area. This finding represents the actual difference between weather and climate: According to National Oceanic and Atmospheric Administration (NOAA), climate is what is being expected from a region, while weather is an actually happening mix of events that happen on a daily basis in the atmosphere. Factors like air pressure, temperature, humidity, wind speed and wind direction etc. have a strong influence on the weather. The weather is mostly happening in the troposphere, which is closest to the Earth's surface. In contrast to that, climate is what is happening long-term in a specific area, e.g. over 30 years. Factors to describe the climate can be different seasons, typical wind patterns or precipitation patterns (NOAA 2020).

Wind speed and the amount of cloud coverage are the most crucial meteorological indicators to influence UHI intensity and its development (Ackermann 1985). Studies show that the amount of cloud coverage and wind speed influence solar radiation and ventilation, which describe the radiative and turbulent conditions in the respective region. These two parameters typically result in a strong correlation with UHI intensity due to their effects on atmospheric stability. The study, carried out in the city of Melbourne, Australia, showed that the UHI intensity was inversely proportional to the fourth root of cloud coverage and wind speed: Increasing both parameters resulted in a significant large UHI intensity development with the highest values during clear to near-clear sky conditions and during calm to low wind speeds (Morris et al. 2001).

Due to the reduction of UHI intensity because of high cloud cover and wind speed, the ideal meteorological conditions for UHI development would be a scenario consisting of a constant sky with calm and clear conditions. These conditions would allow rural surfaces to cool down faster during nighttime than urban surfaces (Ganbar et al. 1998).

Diurnal and seasonal variabilities

Temperature patterns behave differently throughout the day and the year, causing diurnal and seasonal variabilities in UHI effect. Various studies show that the UHI intensity differs over the course of the day, e.g. in Ulaanbaatar, Mongolia, the average

UHI intensity is 1.6 K, with peaks in winter (3.3 K) and in summer (0.3 K), respectively, as in many cities around the world (Ganbar et al. 1998).

In general, UHI intensity is depending on the time of the day and the seasonal conditions, being stronger during nighttime than during daytime (Camilloni et al. 2012).

2.4 Urban morphology

Especially during nighttime, urban geometry has a major impact on UHI effect. Urban geometry, i.e. spacing and dimensions of the buildings, affects wind flow, energy absorption and long-wave radiation back to space. Furthermore, due to the high building density in developed areas, many buildings are fully or partially obstructed by the adjacent construction. These obstructions shape large thermal masses and prevent the buildings from releasing energy and from cooling down during nighttime. This phenomenon is often referred to as “Urban canyon effect” (Figure 3) (Buena de Morias et al. 2019).

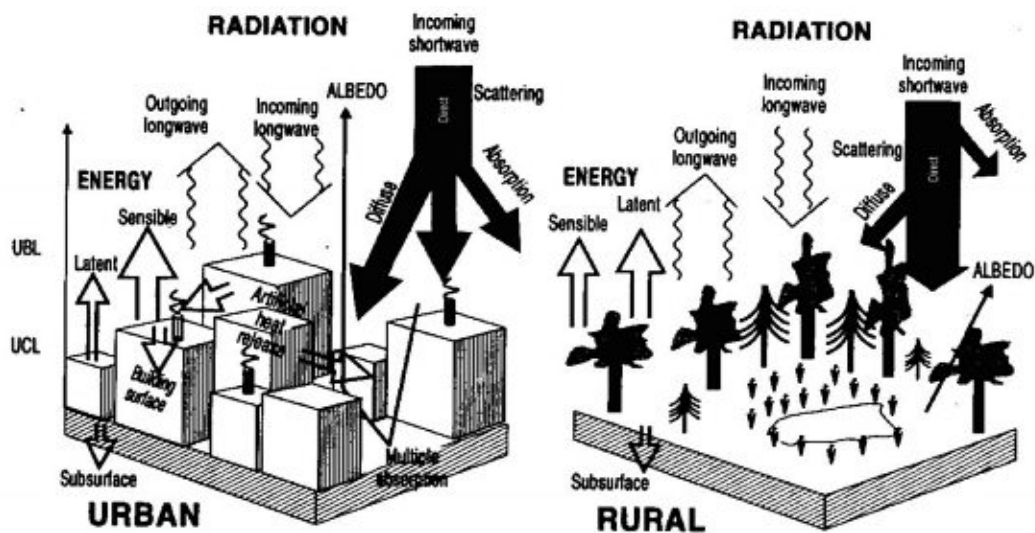


Figure 3: Incident solar radiation in rural areas and urban canyon effect (TERI 2017)

As per Memon et al. (2010), urban canyons – also known as street canyons – characteristic narrow streets in urban areas, shaped by flanking buildings (e.g. skyscrapers) and road courses. Urban canyons separate cities into dense blocks of structures, affecting temperature (sunlight and shade), wind (cross-street vortices), air quality (pollution) and even satellite navigation.

Street canyons are commonly described by aspect ratio AR (-), the quotient of the mean height of the flanking buildings (H) and the street width (W). Air temperature differences between high and low AR (8.0 and 0.5, respectively) are higher during

nighttime (i.e. a difference of 7.5 K) but close to zero during daytime. Furthermore, the decreased ambient wind speed from 4 m/s to 0.5 m/s resulted in a rise of air temperature of 1.3 K. These patterns were obtained resembling one another in urban as well as rural areas, concluding the significance of AR and wind speed in urban canyons on urban heat islands (Memon et al. 2010).

However, urban canyons can have a competing effect: On the one hand, the tall buildings like skyscrapers provide shade to their surroundings, decreasing surface and ambient air temperature and allowing adjacencies to cool down during nighttime. On the other hand, incident solar radiation is reflected and absorbed by the narrowly spaced building façades. This results in lower overall albedo which may increase temperatures again. Generally, urban canyons hardly cool down during nighttime due to the mutual obstructions, impeding heat from being released (EPA 2017).

Summarizing and taking into account the driving forces mentioned above, the reason for UHI effect cannot be summed up in one essential point, but rather in a continuing cycle. The roots of UHI effect lie within a steady process in which demographic patterns are slowly being shifted due to globalization and global social, economic, and ecologic circumstances. As a consequence, rural migration triggers the adaptation of urban areas in order to withstand a relocation of demographic conditions. Hence, cities are forced to adopt changes in their spatial and economic organization such as the implementation of new residential, commercial and industry buildings, expansion of the infrastructural network, supply, as well as providing sufficient living space for the growing number of inhabitants.

3 MATERIALS AND METHODS

3.1 Overview

The second part of this study shall provide a description of the study site and the chosen method in order to conduct the study: The acquired data shall be presented in a comprehensible way in order to follow the deployed methods. The engagement of the repository by computational calculation tools (software, plugins) shall be presented chronologically and hand in hand with the applied formulae and input variables in order to generate meaningful results.

Lastly, the hypothesis shall frame the predictions of the study, and prove whether the results found by the applied method support the predictions.

3.1.1 Study site

Vienna (Lat: 48° 12' 29" N, Lon: 16° 21' 25" E) is the capital city of Austria and one of the nine states of Austria. With 1.9 million inhabitants and 2.6 million with the metropolitan area, Vienna is also the largest city of Austria and occupies about one fifth of Austria's population.

Vienna has an oceanic climate with warm summers and frequent precipitation, reaching the annual peaks in July and August. The average high temperatures are recorded between June and September and lie within a 21 °C to 27 °C range. Viennese winters are dry and cold, having an average temperature at freezing point. On average, snowfall is recorded from November to March. The average annual precipitation of Vienna is 550 mm.

The city is located in the north-east of Austria, at the easternmost extension of the Alps in the Vienna Basin (Figure 4). By the time, the city spans both sides of the Danube river, which crosses the city border in the north and in the south-east. The topography of Vienna is mostly flat to hilly, with an elevation range from 151 m to 542 m. Vienna has a total area of 414.65 square kilometers, making it the largest Austrian city also in terms of area.

The notable biodiversity – including green areas of more than 50 % of the total city area and the Danube river – as well as the dense city center contribute to making Vienna a suitable example area for this study (Taxacher et al. 2016).

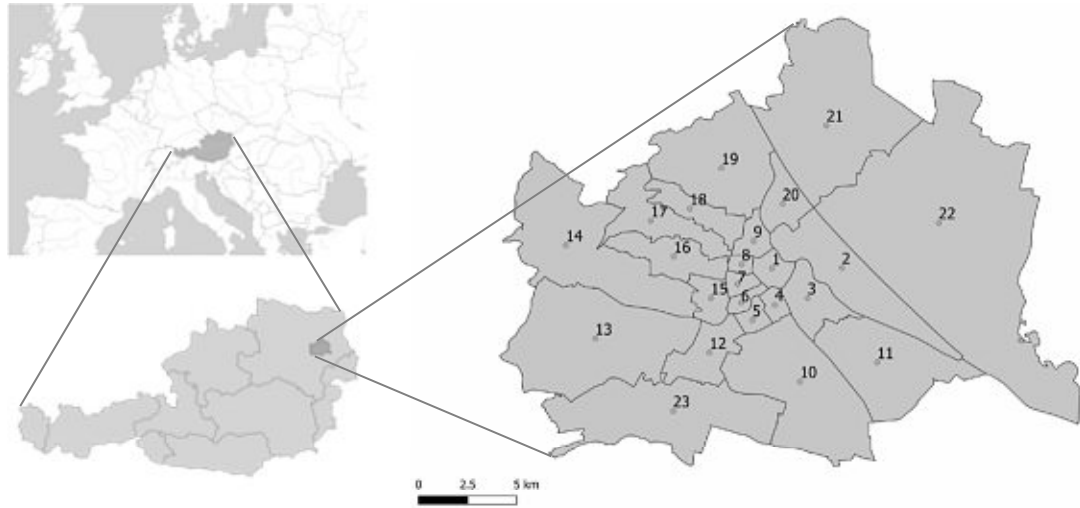


Figure 4: Location of the study area Vienna, Austria (QGIS 2020)

Like many other cities with similar demographic properties, Vienna has experienced increased population growth of about 0.8 % throughout the past years, due to urbanization. The current population growth rate is about 13.1 % compared to 2010, when it was 9.1 %. By 2050, the city of Vienna is expected to have about 2.2 million inhabitants. Patterns like these drastically contribute to harming the thermal circumstances not only in Vienna, Austria, but on the global environmental scale in various cities and urban settings (Statistik Austria 2020).

3.1.2 Data acquisition

In order to get a preliminary overview of the available data, a feasibility check was undertaken in Earth Explorer, provided by the US Geological Service (USGS). The available data was checked beforehand as described below in order to make sure the data is suitable for the study.

To capture surficial changes, Landsat images are used. The Landsat Program is a joint program between NASA and USGS and provides the longest continuous space-based record of the world's surface. Landsat satellites make essential and irreplaceable land use and land cover change information available on the global scale. Furthermore, Landsat contributes to provide essential footage in order to support land managers and policy makers in decision making about global resources and the environment of our planet. The observations provided are synoptic and repetitive footage which is significantly important to inform good decisions in a host of disciplines such as human health, ecosystems, biodiversity, carbon and climate, energy and water management as well as urban growth (USGS 2020).

USGS data can be retrieved via Earth Explorer and requires an USGS account. For this study, the data set "Landsat Collection 1 Level 1: Landsat 8 OLI/TIRS C1 Level-

1" was chosen. For filtering, the city of Vienna was chosen. Alternatively, the target location can be defined by World Reference System 2 (WRS-2), which divides Landsat 8 data into squares, depending on latitudinal and longitudinal information. According to WRS-2 nomenclature, Vienna is located in 190-026, namely path 190 and row 26, respectively, which covers an area of 33,300 square kilometers (180 km by 185 km) (Figure 5).



Figure 5: Dimensions of Landsat 8 images at WRS-2 190-026 (Earth Explorer 2020)

To avoid distortion in the data set, the maximum of valid cloud coverage shall be below 5%. For the data set of the past condition, the time span was set to earlier than 2015; for the present condition, the time range for the data was set from 2019 to 2020. For both data sets, the months April to September were chosen in order to avoid snow coverage.

Past condition

The Landsat 8 data recordings started in the year of 2013, thus the oldest eligible data sets for the past condition were recorded from January 2013 onwards. In order to have the greatest difference possible between the past and present scenario, the five oldest data sets available were chosen for comparison. Considering these requirements, the following data sets were found to be valid for the study:

- i) 2014-07-07
- ii) 2014-05-20
- iii) 2013-09-06
- iv) 2013-08-05

v) 2013-06-18

Due to the high cloud coverage rate and the date of recording, both data sets from 2014 were excluded from further selection. Via “quick view” tool in Earth Explorer, the remaining data sets were again undertaken a visual check with regard to image brightness, contrast, details and possible outliers. The evaluation matrix is presented in Table 3.

Table 3: Evaluation matrix for the selection of the data set for the past condition (Point scale: Good = 2 pt, OK = 1 pt, bad = 0 pt)

Criterion	2013-09-06	2013-08-05	2013-06-18
Brightness	Good	OK	Bad
Contrast	OK	Good	OK
Details	Good	OK	OK
Outliers	OK	OK	Bad
Sum	5	4	2

The remaining data set to fulfill the visual check most adequately (i.e. reaching the highest point score) and to be chosen for the study was data set 2013-09-06.

Present condition

For the present conditions, the timely filter was set to 2019 until 2020, again, with the searching months April to September. Considering a cloud coverage of 5 % at maximum, the search showed four eligible results for Vienna location, 190-026, as follows.

- i) 2020-09-09
- ii) 2020-08-08
- iii) 2020-04-02
- iv) 2019-06-03

Similarly as for the previous scenario, the present data sets were also undertaken a visual check with regard to brightness, contrast, details and possible outliers. The scoring for the data sets as well as the results are presented in the evaluation matrix below (Table 4).

Table 4: Evaluation matrix for the selection of the data set for the present condition (Point scale: Good = 2 pt, OK = 1 pt, bad = 0 pt)

Criterion	2020-09-09	2020-08-08	2019-04-02	2019-06-03
Brightness	Good	Good	Good	Bad
Contrast	OK	Good	Good	Bad
Details	OK	OK	OK	Bad
Outliers	Good	Bad	Bad	OK
Sum	6	5	5	1

The data set to fulfill the visual check most adequately (i.e. reaching the highest point score) and to be chosen for the study was data set 2020-09-09.

It was found that the two chosen data sets were both recorded during early September in the respective years of 2013 and 2020. Considering two data sets recorded at a similar date may be beneficial for the study due to similar climatic conditions. Although the weather circumstances may differ from one another, the chosen data sets were recorded with the least difference possible in time in the respective year, which allows for better comparison of the results.

Download with Semi-Automated Classification plugin

Once the most adequate data sets have been chosen, the data acquisition process can be shortened and the data can be downloaded directly in the Semi-Automated Classification plugin (SCP), developed by Luca Congedo. Downloading the imagery through SCP in QGIS allows for a preview of the satellite image right in the study area in order to prevent redundancies or shifting in the area of interest. Apart from the raw satellite images, the MTL file can be acquired, which will be necessary for calculations at a later stage of the study.

Moreover, by engaging SCP for data acquisition, the user is able to decide what bands of the data should be deployed instead of bulk-downloading the whole imagery set, which usually require around 1 gigabyte of storage space. Further, SCP not only provides downloading Landsat, but also data from other satellites such as SENTINEL and ASTER.

According to USGS, the nomenclature of the Landsat products consists of various information about the chosen band set and is generated as presented in Table 5 (USGS 2020).

Table 5: Landsat product identification (USGS 2020)

Indicator	Landsat Product Identifier
Nomenclature	LXSS_LLLL_PPPRRR_YYYYMMDD_yyyymmdd_CC_TX
L	Landsat
X	Sensor (C = OLI/TIRS Combined, O = OLI only, T = TIRS only, E = ETM+, T = TM, M = MSS)
SS	Satellite (07 = Landsat 7, 08 = Landsat 8)
LLLL	Processing correction level (L1TP = Precision terrain, L1GT = Systematic terrain, L1GS = Systematic)
PPP	WRS path
RRR	WRS row
YYYYMMDD	Acquisition year (YYYY)/Month (MM)/Day (DD)
yyymmdd	Processing year (yyyy)/Month (mm)/Day (dd)
CC	Collection number (01, 02)
TX	Collection category (RT = Real-Time, T1 = Tier 1, or T2 = Tier 2)
Examples	LC08_L1GT_029030_20151209_20160131_01_RT LE07_L1TP_016039_20040918_20160211_01_T1 LT04_L1GS_017036_19821115_20160315_01_T2 LM01_L1GS_017039_19760131_20160225_01_T2

It has to be noted that the suffix of the Landsat data sets is crucial for processing the bands in GIS software. For example, data sets with the suffix -RT (Real Time) cannot be processed in the SCP. RT is one of three tiers for categorizing scenes with Landsat. According to USGS, RT has the following features:

- i. Holds newly acquired Landsat scenes
- ii. Landsat 8 thermal data may be misaligned with OLI data
- iii. Landsat 7 uses predicted geometry until definitive models are calculated

RT can be useful in monitoring events and natural disasters, where near RT data is critical. In general, Landsat 8 OLI data is very accurate, however, the thermal bands require additional processing before the scene can be placed in the final tier. This process is applied within 16 days after acquisition. The data is then categorized into Tier 1 or Tier 2. Tier 1 has the highest quality data with a maximum RMSE of 12 meters. This might cause severe deviations in some scenes, especially those from

previous satellites or with a RMSE of more than 12 meters. The causes of high RMSE might be due to significant cloud cover and/or insufficient ground control points during sensing (USGS 2017).

A summary of the retrieved data is provided in Table 6.

Table 6: Overview of the used satellite data from Landsat 8 (USGS 2020)

ID	Time step	Acquisition date	Path/ Row	Cloud coverage	Pixel size [m x m]
LC08_L1TP_190026_2013_0906_20200502_01_T1	Past	2013-09-06	126/90	< 1 %	30 x 30
LC08_L1TP_190026_2020_0909_20200918_01_T1	Present	2020-09-09	126/90	< 1 %	30 x 30

Regarding calculation accuracy, it is crucial to compare two satellite data sets which were acquired at similar seasonal and weather conditions. By taking past and present data sets from early September into calculation, this criterion is met, and later calculations are qualified for being reasonably compared.

3.2 Land use/land cover classification

QGIS (formerly QuantumGIS) is an open source GIS software for displaying, editing, generating and analyzing geographical data, developed in 2002 by the QGIS Development Team (QGIS 2020). For the study, QGIS version 3.10 “A Coruña” was used.

Moreover, World Geodetic System (WGS) 84 EPSG:4326 was chosen as a coordinate system, which is also being used for GPS satellite navigation systems and for the North Atlantic Treaty Organisation (NATO) military geodetic surveying (EPSG 2007).

The land cover classifications of the past and present condition were undertaken with Semi-Automatic Classification Plugin (SCP). The land use/land cover was classified into the following categories: water, built-up, vegetation and bare soil. The land cover classification consists of an algorithm training, which is an iterative phase, and the classification itself. The algorithm training contains photointerpretation and regions of interest (ROI) creation, assessment of spectral signature separability, accuracy assessment and the classification preview (Congedo 2020).

In the latest version of SCP, Version 7, the data can be downloaded right in the SCP mask under “Download products”, which requires a valid user account for USGS Earth Explorer. The search parameters for the past and present conditions were set as displayed in Table 7.

Table 7: Search parameters for Landsat 8 download in SCP (QGIS 2020)

Parameter	Value
UL X (Lon)	16.15
UL Y (Lat)	48.35
LR X (Lon)	16.60
LR Y (Lat)	48.07
Products	L8 OLI/TIRS
Date	2013-09-06 and 2020-09-09
Max. cloud cover	10 % (lowest value possible)
Download options	Landsat bands 2, 3, 4, 5, 6, 7, MTL file

After downloading, the bands were clipped in order to specify the study area, meaning that the 180 x 185 km satellite images were cropped according to the study area down to a 30 x 35 km, spaciouly covering the north-south and east-west extensions of the city. For this purpose, a new band set has to be created in the “Band set” tool. Then the band set could be clipped by “Clip multiple rasters” function in the “Preprocessing” tool. As a next step, the clipped bands were converted to reflectance, which was done via “Landsat” tool in “Preprocessing”. As an input, the clipped file and the automatically generated metadata (MTL) file were chosen. The MTL file contains the required information for the conversion to reflectance.

Additionally, the “Dark Object subtraction 1” (DOS1) atmospheric correction was applied. The DOS1 algorithm corrects the image band in comparison to top-of-atmosphere (TOA) and surface reflectance values on the blue and green bands as shown in Figure 6.

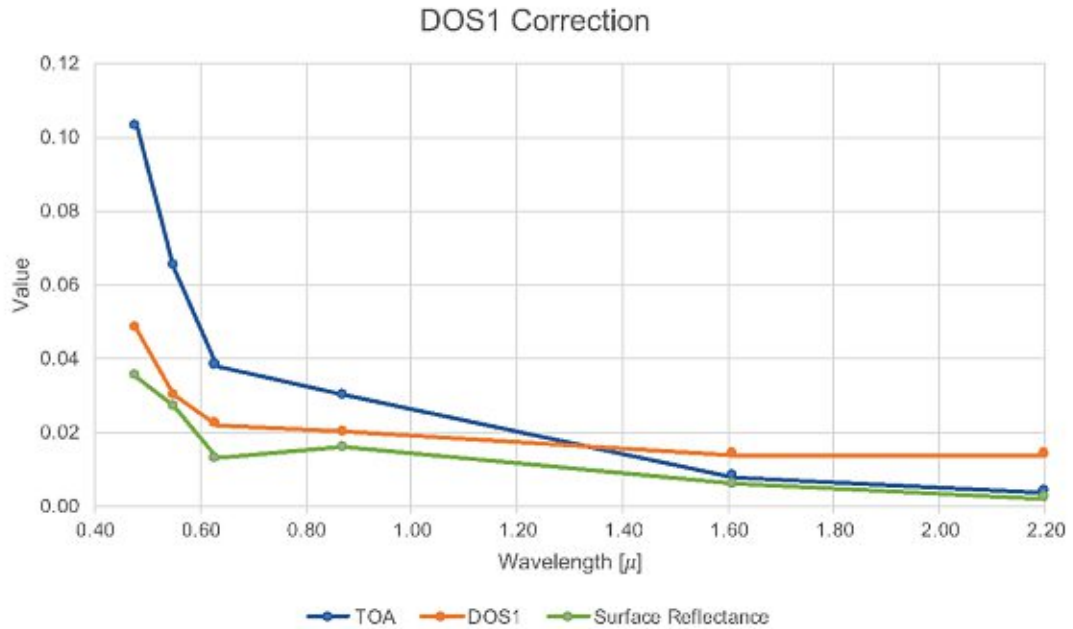


Figure 6: DOS1 Correction by SCP (Congedo 2020)

The converted bands were automatically loaded into QGIS with “RT” as a prefix. With these bands a new band set was created, which is the input for the classification. The wavelength settings were set to Landsat 8 OLI and μm as the wavelength unit (Table 8).

Table 8: Center wavelength for Landsat 8 bands B2-B7 (QGIS 2020)

Band name	Center wavelength [μm]
B2	0.48
B3	0.56
B4	0.655
B5	0.865
B6	1.61
B7	2.2

To classify the images, a training input was generated. The training input consists of the macro classes (MC) water, built-up, vegetation, and bare soil, and subdividing classes (C) as represented in Figure 7.

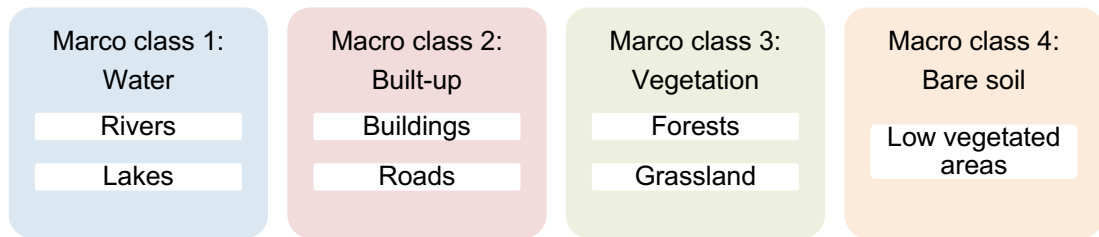


Figure 7: Macro classes and classes for the training input in SCP (Congedo 2020)

By applying the region growing algorithm in QGIS, the regions of interest (ROI) were selected and assigned to the respective macro classes and classes as in Figure 7.

The region growing algorithm is defined by the spectral distance (0.1), minimum size (1 pixel) and maximum ROI width. As shown in Figure 8, the region growing algorithm assigns all pixels within the maximum ROI width (a) and the spectral distance threshold (b) to the chosen pixel (c, orange pixel) and creates the growing region (d).

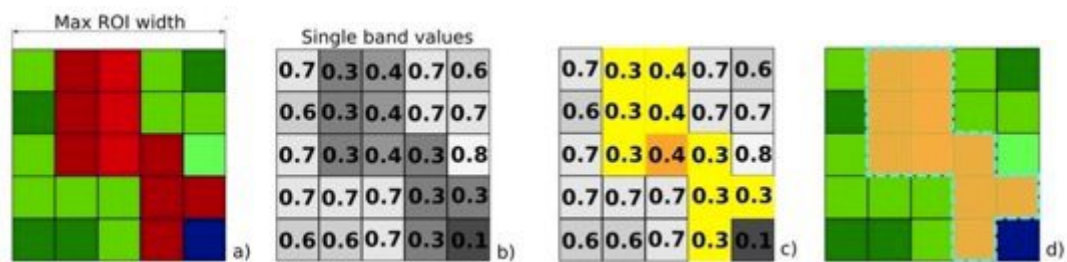


Figure 8: Region growing algorithm (Congedo 2020)

The ROIs were saved in the ROI signature list. For the classification, several approaches were made. The first attempt was an initial classification with ten ROIs in order to test the functionality of the SCP in QGIS. In order to apply the classification to both past and present conditions similarly, a training input file with 49 evenly distributed training inputs was generated and used for both classifications, 2013 and 2020.

As a classification algorithm for this study, Maximum Likelihood algorithm was chosen. It calculates the probability distributions for the classes related to Bayes' theorem, assessing if a pixel can be assigned to a given (macro) class. Pixels with a probability of less than the given threshold value (max. 100) remain unclassified. In contrast to that, Minimum Distance algorithm and Spectral Angle Mapping algorithms would assign pixels as unclassified if the distance or the spectral angle distance, respectively, were greater than the given threshold value (Congedo 2020).

3.3 Land use/land cover prediction

Models for Land Use Change Evaluation (MOLUSCE) is a plugin for QGIS which provides a set of algorithms for land use change simulations such as Artificial Neural Network (ANN) or Weight of Evidence (WoE). MOLUSCE takes classified land use/land cover raster images for time period A (past) and for period B (present) and generates classified land use/land cover raster images for time period C (future). In order to run simulations, MOLUSCE requires same size format (pixel size) and extent raster images.

Additionally, at least one explanatory spatial variable raster image is required to georeference the scenarios, e.g. road map, river map, tree cadaster, “distance to road” map, “distance to river” map.

In this study, a “distance to district center” map was provided in order to spatially reference the city map (NextGIS 2014).



Figure 9: Spatial variable map of Vienna: distance to district center (QGIS 2020)

The greyscale in Figure 9 displays the distance in each of the 23 federal districts of Vienna to its respective center: The lighter the shade, the farther away located is the respective pixel from the district center. The spatial variable map helps the algorithm behind MOLUSCE plugin to reference basepoints in order to assign the corresponding surface types correctly in the course of the classification. It is possible to provide more than one spatial variable map in order to increase the level of accuracy of the classification.

Due to the temporal difference of seven years between the two reference conditions, the simulation process was additionally executed five times after the 2020 scenario in order to reach the target year 2055. The projection was calculated with 5000 iterations and an inaccuracy of 0.09 %.

MOLUSCE plugin implements the following process:

- i. Takes past and present classified raster images and explanatory variable map
- ii. Trains a model that predicts land use/land cover changes from past to present
- iii. Predicts future land use/land cover changes using the derived model, current state of land use/land cover and current factors provided in the explanatory variables

The past and present raster images are analyzed through overlaying process on the land use/land cover data. As a result, MOLUSCE creates a “changes map”, which identifies the changes of the land use/land cover classification from past to present scenario. MOLUSCE is then able to calculate a transition matrix of the probability of change between the two scenarios. The output of the module is a transition potential raster of the model, “certancy” map (displaying the difference between the two largest potentials), and the simulation results, which is the predicted future land use/land cover classification (NextGIS 2014).

3.4 Land surface temperature calculation

In order to retrieve land surface temperature, additional input parameters are required beforehand: Normalized Difference Vegetation Index (NDVI) is a versatile vegetation index to evaluate the vegetation and dynamic of the vegetation coverage change. The calculation method of NDVI changes respectively to the number and type of bands of the satellite. For Landsat 8 data, NDVI is calculated by Equation (2)

$$NDVI = \frac{NIR - Red}{NIR + Red} = \frac{Band5 - Band4}{Band5 + Band4} \quad (2)$$

where band 4 has a wavelength of 0.630 – 0.680 μm and Band 5 has a wavelength of 0.845 – 0.885 μm . Both bands allow a resolution of 30 by 30 meters (i.e. pixel size). Generally, NDVI represents a surface’s “greenness”, derived from a vegetation’s density and productivity. NDVI typically ranges from -1 to 1, where a higher value indicates a more vegetated area, for example forests, grass and farmland. Water bodies such as rivers and lakes have a close to -1 NDVI value (Yang et al. 2017).

On base of NDVI threshold method, emissivity can be derived for the 10-12 μm range of Landsat 8, band 10 (10.8 μm).

According to Sobrino et al. (2001), thresholds of NDVI are as summarized in Table 9.

Table 9: NDVI threshold method (Sobrino et al. 2001)

Threshold criterion	Value
NDVI < 0.2	The pixel is considered as bare soil; emissivity is derived from reflectance.
NDVI > 0.5	The pixel is considered as fully vegetated, where a constant value of 0.99 for emissivity is assumed.
0.2 ≤ NDVI ≤ 0.5	The pixel consists of soil and vegetation and has to be calculated.

The mathematical base of NDVI threshold method for calculating emissivity is represented in Equation (3) (Sobrino et al. 2001).

$$\varepsilon = \begin{cases} \varepsilon_s, & NDVI < NDVI_{min} \\ \varepsilon_v P_v + \varepsilon_s(1 - P_v) + d\varepsilon, & NDVI_{min} \leq NDVI \leq NDVI_{max} \\ \varepsilon_v P_v + d\varepsilon, & NDVI > NDVI_{max} \end{cases} \quad (3)$$

Equation (4) provides vegetation proportion for NDVI threshold method based on minimum and maximum NDVI values (Sobrino et al. 2001).

$$P_v = \left[\frac{NDVI - NDVI_{min}}{NDVI_{max} - NDVI_{min}} \right]^2 \quad (4)$$

$$NDVI_{max} = 0.5 \quad \text{and} \quad NDVI_{min} = 0.2$$

Equation (5) provides a good approximation for the effect of the geometrical distribution of the natural surfaces and also the internal reflections. F is a shape factor with a mean of 0.55 (Sobrino 1989).

$$d\varepsilon = (1 - \varepsilon_s)(1 - P_v) F \varepsilon_v \quad (5)$$

The calculation base for emissivity can be concluded by Equation (6)

$$\varepsilon = m P_v + n \quad (6)$$

with input parameters as per Equations (7) and (8) (Sobrino et al. 2001).

$$m = \varepsilon_v - \varepsilon_s - (1 - \varepsilon_s) F \varepsilon_v \quad (7)$$

$$n = \varepsilon_s + (1 - \varepsilon_s) F \varepsilon_v \quad (8)$$

Emissivity values can be assumed as $\varepsilon_v = 0.99$, $\varepsilon_s = 0.97$, $m = 0.004$ and $n = 0.986$, resulting in the final expression for land surface emissivity as per Equation (9) (Sobrino et al. 2001).

$$\varepsilon = 0.004 P_v + 0.986 \tag{9}$$

The process displayed by the white fields in Figure 10 describes the baseline of the calculation of land surface temperature with Mono-window algorithm (MWA) according to Qin et al. (2001).

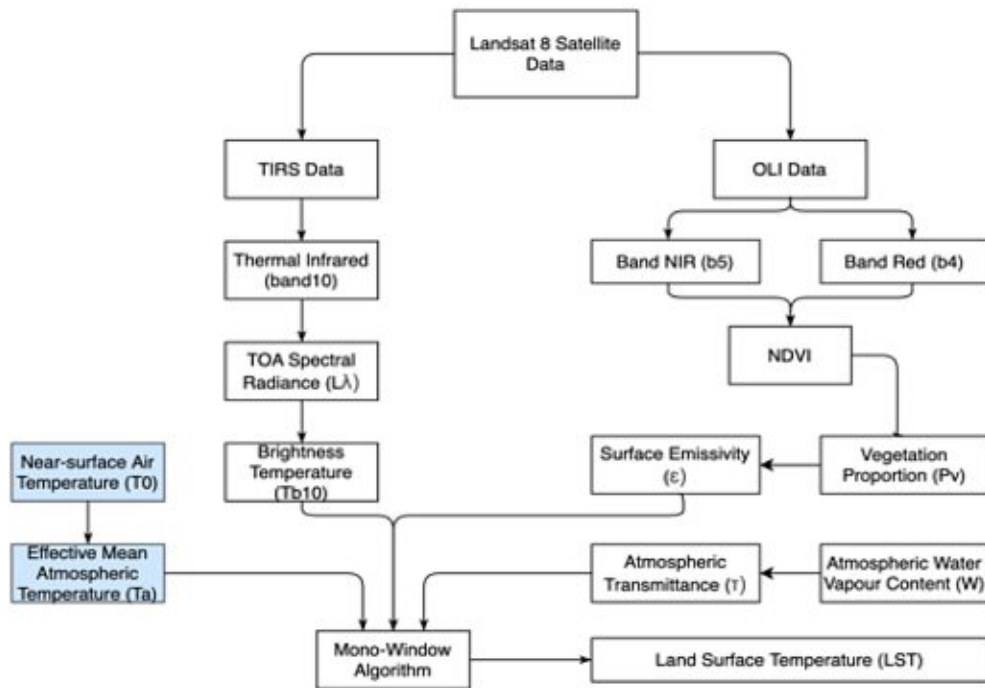


Figure 10: Modified Mono-window Algorithm with additional input parameters (T_{10} and T_a) (Wang et al. 2019)

By integrating near-surface air temperature (T_0) and effective mean atmospheric temperature (T_a) (blue fields) as additional input values into MWA, land surface temperature can be calculated with Equation (10), improved and adapted to Landsat 8 band 10

$$LST = \frac{a_{10}(1 - C_{10} - D_{10}) + (b_{10}(1 - C_{10} - D_{10}) + C_{10} + D_{10})T_{10} - D_{10}T_a}{C_{10}} \tag{10}$$

with a_{10} and b_{10} according to Table 8 (Wang et al. 2015).

Table 10: a_{10} and b_{10} input parameters depending on the temperature range (Wang et al. 2015)

Temperature range	a_{10}	b_{10}	R_2
20 - 70 °C	-70.1775	0.4581	0.9997
0 - 50 °C	-62.7182	0.4339	0.9996
-20 - 30 °C	-55.4276	0.4086	0.9996

C_{10} and D_{10} are the internal parameters for the improved algorithm and can be calculated by Equations (11) and (12).

$$C_{10} = \varepsilon_{10} \times \tau_{10} \quad (11)$$

$$D_{10} = (1 - \tau_{10}) \times [1 + (1 - \varepsilon_{10}) \times \tau_{10}] \quad (12)$$

The effective mean atmospheric temperature can be estimated by the linear relation between the respective location and near-surface air temperature according to Table 11.

Table 11: Relationship between T_o and T_a depending on the region (Wang et al. 2015)

Atmosphere	Linear Relations Equations
Tropical model	$T_a = 17.9769 + 0.9172 T_o$
Mid-latitude summer	$T_a = 16.0110 + 0.9262 T_o$
Mid latitude winter	$T_a = 19.2704 + 0.9112 T_o$

As per Qin et al. (2001), near-surface air temperature can be derived from local meteorological observation stations and calculated by Equation (13).

$$T_{0,t} = T_{min} + (T_{max} - T_{min}) \sin \left[\pi \left(t + \frac{t_{dl}}{2} - 12 \right) / (t_{dl} + 2t_{Tmax}) \right] \quad (13)$$

T_{min} and T_{max} are the daily minimum and maximum near-surface air temperatures, respectively, and were obtained from weather stations in and around Vienna (Figure 11 and Figure 12) (Kachelmann 2020).

The input parameters for the near-surface air temperature $T_{0,t}$ and time t are summarized in Table 12.

Table 12: Input parameters for near-surface air temperature (Qin et al. 2001)

Parameter	Explanation	Value
t	Time of satellite overpass (11:45 a.m. CEST, Vienna local time, rounded down to full hour)	11
t_{dl}	Day length in hours	13
t_{Tmax}	Number of hours between local solar noon and the time of T_{max}	5

It has been found that for the past scenario of 2013, observation data was only available for the weather stations Wien-Hohe Warte and Wien-Schwechat.

For the present scenario, 2020, all seven available weather stations provided observation data (Table 13).

Table 13: Relevant weather stations for the study (Kachelmann 2020)

Weather station name	List name in Appendix 2
Wien-Mariabrunn	MB
Wien-City	City
Wien-Hohe Warte	HW
Wien-Unterlaa	UL
Wien-Donaufeld	DF
Wien-Schwechat	SW
Großenzersdorf	GD

T_0 was calculated and spatially interpolated for the past and present scenarios, respectively (Appendix 2). The respective locations of the available weather stations can be seen in Figure 11 and Figure 12.



Figure 11: Spatial interpolation for T_0 in 2013 (QGIS 2020)

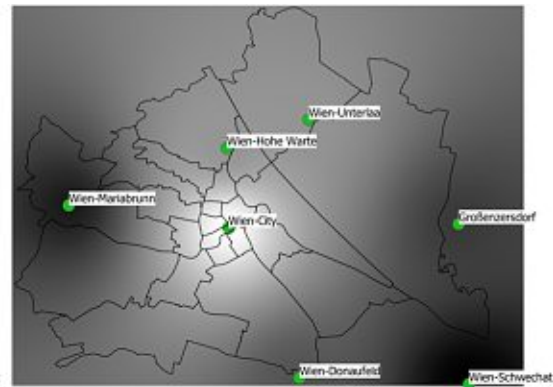


Figure 12: Spatial interpolation for T_0 in 2020 (QGIS 2020)

Brightness temperature, T_{10} , can be calculated from band-specific thermal conversion constants (K_1 , K_2), spectral radiance (L_{λ}), radiance rescaling factors (M_i , A_i), the quantized and calibrated standard product pixel value Q_{cal} . These values can be found in the respective metadata (MTL) file of the corresponding band set and are summarized in Table 14.

Table 14: Radiance rescaling factors and band-specific thermal conversion constants (Congedo 2020)

	2013	2020
A_L	0.1	0.1
M_L	3.342 * 10 ⁻⁴	3.342 * 10 ⁻⁴
K₂	1321.0789	1321.0789
K₁	774.8853	774.8853

The mathematical definition for brightness temperature (T_{10}) and spectral radiance (L_{λ}) are provided in Equations (14) and (15) (Sobrino et al. 2001).

$$T_{10} = \frac{K_2}{\ln\left(\frac{K_1}{L_{\lambda}} + 1\right)} \quad (14)$$

$$L_{\lambda} = M_i Q_{cal} + A_i \quad (15)$$

According to Wang et al. (2015), Table 15 can be used for the estimation of the atmospheric transmittance.

Table 15: Water vapor content and transmittance estimation equation (Wang et al. 2015)

Atmosphere	Water Vapor Content	Transmittance Estimation
	[g/m ²]	Equation
Mid-latitude summer	0.2 – 1.6	$\tau_{10} = 0.9184 - 0.0725w$
	1.6 – 4.4	$\tau_{10} = 1.0163 - 0.1330w$
	4.4 – 5.4	$\tau_{10} = 0.7029 - 0.0620w$
Tropical model	0.2 – 2.0	$\tau_{10} = 0.9220 - 0.0780w$
	2.0 – 5.6	$\tau_{10} = 1.0222 - 0.1310w$
	5.6 – 6.8	$\tau_{10} = 0.5422 - 0.0440w$
Mid-latitude winter	0.2 – 1.4	$\tau_{10} = 0.9228 - 0.0735w$

For this study, the mid-latitude summer scenario was taken into consideration. In order to identify the transmittance estimation equation that fit the scenario most closely from the three possible approaches provided, water vapor content w in g/cm² was computed empirically:

As per Equation (16), variable w is the total water vapor content in the atmospheric column up to the sensor, w_0 is the water vapor content at the ground of the

atmosphere, and Rw_0 is the ratio of water vapor content at the first layer to the total (Wang et al. 2015).

$$w = \frac{w_0}{Rw_0} \quad (16)$$

The water vapor content at the ground can be derived by Equation (17)

$$w_0 = \frac{H * E * A}{1000} \quad (17)$$

with H as air humidity at the ground, E as the saturation mix ratio of water vapor and air for a specific air temperature, and A as the air density at the specific air temperature (Wang et al. 2015).

Table 16 provides input parameters for E and A according to the respective specific air temperatures.

Table 16: E and A input parameters depending on air temperature (Wang et al. 2015)

T [°C]	45	40	35	30	25	20
E [g/kg]	66.33	49.81	37.25	27.69	20.44	14.95
A [kg/m³]	1.11	1.13	1.15	1.17	1.18	1.21
T [°C]	15	10	5	0	-5	-10
E [g/kg]	10.83	7.76	5.50	3.84	2.52	1.63
A [kg/m³]	1.23	1.25	1.27	1.29	1.32	1.34

The average temperature and humidity values for September in Vienna were found to be 26.1 °C and 67 %, respectively (Time and Date AS 2021).

By interpolating the two according to Table 16, the input values for the water vapor content calculation could be identified. The interpolated values are E = 22.05 and A = 1.178. The third input variable is Rw_0 and was interpolated according to Wang et al. (2015), resulting in 0.6834 for mid-latitude summer.

By taking the mentioned values into consideration, the water vapor content resulted in 2.55 g/m² as per Equation (16). Subsequently, transmittance (τ_{10}) was estimated by equation 1.0163 – 0.133w (Table 15).

All calculations based on the water vapor content were executed by utilizing “Raster calculator” in QGIS, a built-in computation tool that produces one value per pixel of a raster image. A clipped raster of the study area consists of approximately 460,000 pixels, accounting for a large amount of information for each image.

3.5 Land surface temperature projection

For the purpose of projecting the calculated land surface temperature results of the past and present scenario into the future, a linear approach was chosen. In principal, simple linear regression is used for modelling the two-dimensional relationship between the dependent and independent variables. It is commonly used for prediction, forecasting or for the purpose of identifying the strength of the relation between the dependent and the independent variable(s). By identifying the line (i.e. trend line) that fits the input data most accurately, the movement of the dependent variable can be estimated (Zou et al. 2003).

The linear regression line generated in this study consists of one dependent variable (i.e. land surface temperature) and one independent (or explanatory) variable (i.e. time). The function is described by Equation (18)

$$y = a + bx \quad (18)$$

where x is the independent variable and y is the dependent variable. The intercept of the line at the second axis is a , and b is the slope of the line (Yale University 1997).

For each of the approximately 460,000 observed pixels per raster image, two observed land surface temperature output values are available: past and present. Thus, the observed values were extrapolated for predicting the land surface temperature of the future scenario.

3.6 Hypothesis

Previous research in the field of urban microclimate was undertaken, leading to the effect of urban heat islands. Engaging GIS in microclimate studies is a widespread method to gain insight on the development of urban areas. Remote sensing and therefore using real time spatial data considering the actual building blueprint and urban morphology contributes to the state of the art and improves the results.

The research question to be answered in this study is:

How can GIS be used to predict future land surface temperature in urban areas? And, subsequently, to what extent is land use/land cover change substantially related to urban heat island effect? According to the results, what other key indicators play a crucial role in the change of urban microclimate?

4 RESULTS

4.1 Post-processing

The change in land use/land cover of the reference years and the projected event was displayed over time as well as in dependence on the respective class. Graphical illustrations shall allow for the representation of timely dependent development of land use/land cover change. A linear regression model was used to evince the relationship between time and the mean temperature increase of impervious surfaces over time.

The land surface temperature results were statistically interpreted and compared in time- and class-dependent graphs.

The analysis was executed with QGIS built-in raster and vector analysis tools, sampled points, statistical functions, as well as Microsoft Excel and Matplotlib functions in Spyder for Python 3.9.

Additionally, in order to assess the spatial distribution of the classification, a map with the numbered districts of Vienna is provided in Appendix 1.

4.2 Land use/land cover

The respective areas of the classified regions considering water surfaces, built-up areas, vegetated areas and bare soil, as well as the corresponding percentage of the city's total area (414.6 ha) were extracted from QGIS via "Raster layer unique values report". Table 17 provides the results of the classification, subject to the respective macro classes.

Table 17: Summary of the land use/land cover classification of past, present and future scenarios (in hectare and percent)

LULC class	Area 2013		Area 2020		Area 2055	
	(ha, %)	(ha, %)	(ha, %)	(ha, %)	(ha, %)	(ha, %)
Water	15.3	3.7 %	15.5	3.7 %	15.0	3.6 %
Built-up	180.8	43.6 %	195.6	47.2 %	198.9	51.4 %
Vegetation	183.6	44.3 %	182.1	43.9 %	182.1	40.5 %
Bare soil	34.9	8.4 %	21.4	5.2 %	18.6	4.5 %
Total	414.6	100 %	414.6	100 %	414.6	100 %

The land use/land cover classification of the past and present scenario showed a percentual distribution of 3.7 % water area for both scenarios. Further, it resulted in 43.6 % and 42.7 % built-up area, 44.3 % and 43.9 % vegetated area, as well as 8.4 % and 5.2 % bare soil, respectively. The land use/land cover classification for the predicted scenario of 2055 resulted in a distribution of 3.6 % for water surfaces, 51.4 % built-up area, 40.5 % vegetated area and 4.5 % bare soil.

The majority of the water surface is distributed over the Danube river and its branches and tributaries, although a small number of lakes and ponds was identified over the city. It can be seen that the Danube river area is separated by several built-up area "stripes". These stripes can be identified as two-lane and four-lane bridges.

For all three conditions, the highest density of built-up area was identified in the districts 1-12, 15, 16, 18, 20 and 23, which corresponds either to the city center or areas of residential or commercial use as well as traffic areas (Figure 13).

The districts 13, 14, 17 and 19 are covered with 30 to 50 % of vegetated area. Especially the districts within the "Gürtel" area experience the highest density of impervious surfaces. The areas around Prater theme park, Lainzer Tiergarten, Lobau and Heiligenstadt showed the highest vegetated areas. These areas are mostly covered by forest. Apart from that, some additional green areas, primarily covered

with grass, were identified in Schönbrunn, Wienerberg, Augarten, and Donauinsel, which is an elongated “island” between the two river courses of Neue Donau.

The majority of bare soil areas was identified in the city’s North, in 21st and 22nd district, as well as in the south of the city, in the 10th district. This distribution is in line with the agricultural land use in and around the city of Vienna, for example in Stammersdorf and Ober- and Unterlaa. A map overview highlighting the districts and meaningful locations of the city is provided in Appendix 1.

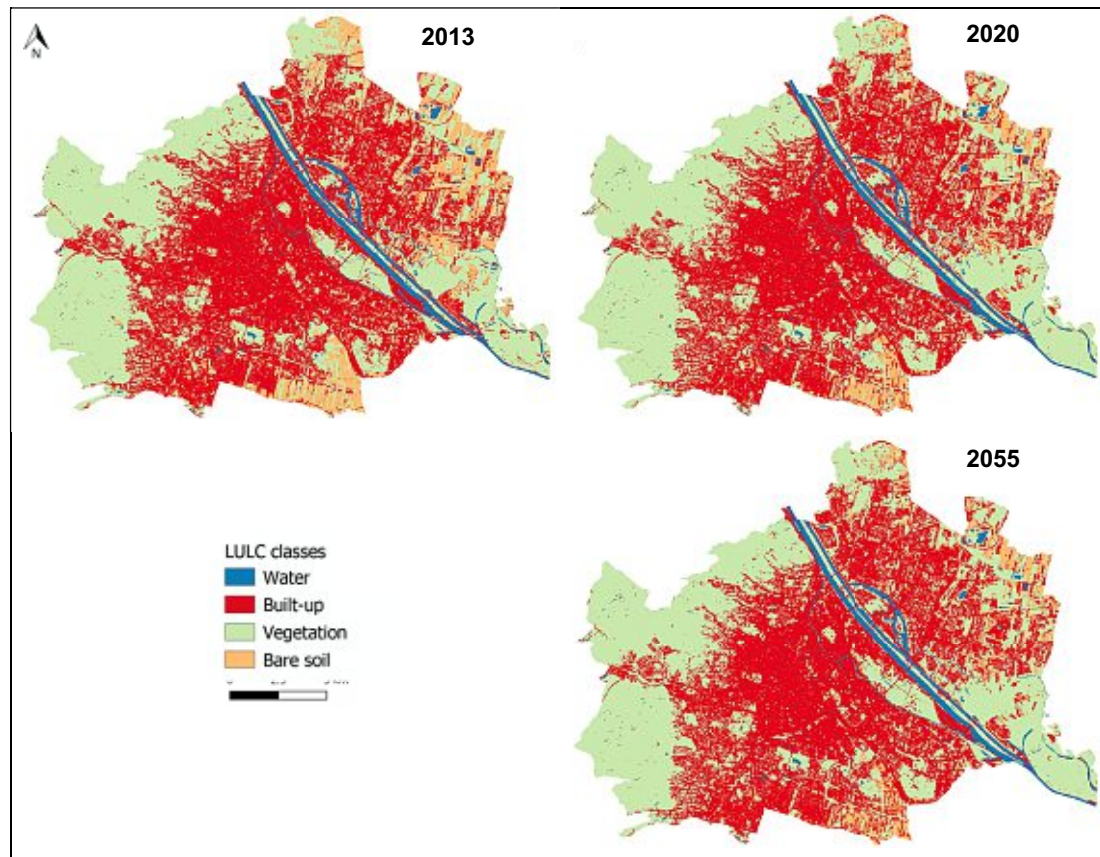


Figure 13: LULC classification of Vienna (QGIS 2020)

In comparison to 2013, the land use/land cover classification of 2020 shows a slight densification of the built-up area in the city center as well as in the outer districts of the city (+ 8.2 %). Moreover, the 2020 classification evinces a drastic decrease (- 61.5 %) of the bare soil areas, especially in the northern part of the city. Both reference years showed a small amount of built-up classified spots, evenly distributed over the forest regions (i. e. eastern and western parts of the city).

The course of the land use/land cover classification for the three conditions is represented zone-wise in Figure 14.

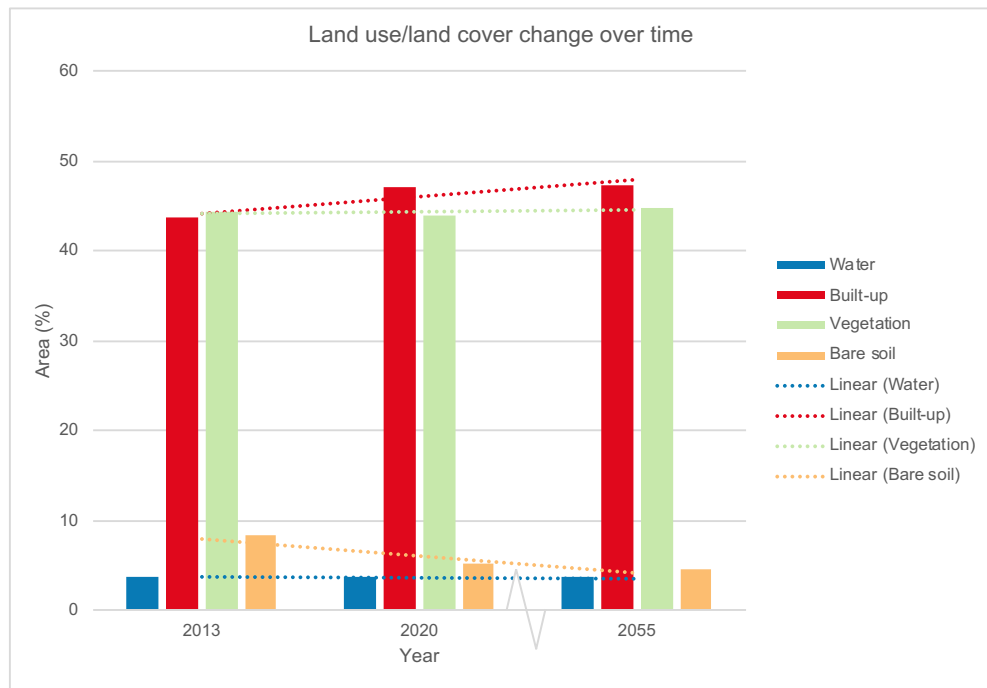


Figure 14: Change of land use/land cover area over time (MS Excel 2021)

Regarding the future condition, the water surface remained mostly the same and the built-up area has increased significantly by 8.9 %. The vegetated and bare soil areas experienced a decrease of 8.4 % and 15.6 %, respectively. It has been found that the MOLUSCE algorithm erased the sparsely distributed small built-up areas in the eastern and western forest areas of the city and overall densified the vegetated and built-up areas.

4.3 Land surface temperature

The minimum, maximum and mean results of the land surface temperature calculations for past, initial and future scenario are summarized in Table 18 and will be further explained in the course of the following points.

Table 18: Summary of the land surface temperatures of 2013, 2020 and 2055 (QGIS 2020)

Scenario	LST (°C)		
	Min.	Mean	Max.
2013	1.67	15.85	29.30
2020	2.55	16.21	29.41
2055	6.90	17.99	31.85

It is notable, that the minimum temperature values for past and present scenarios with 1.67 °C and 2.55 °C, respectively, significantly lie below the typical temperature range, considering seasonal and diurnal conditions. This discrepancy will be further discussed in section 5.2.

The land surface temperature results for the past condition (i.e. 2013) show a mean of 15.9 °C. The minimum and maximum values are 1.7 °C and 29.3 °C, respectively. Interpreted with regard to the land use/land cover classes, the water and vegetated areas show mean surface temperatures of 12.3 °C and 14.7 °C on average, while the built-up and bare soil surface exceed those values of more than 2 K, with 16.6 °C and 17.1 °C, respectively. The lowest temperatures can be obtained in the forest regions in the eastern and western parts of the city, as well as in the water area of the Danube river. It can be concluded that, additionally to the city center, the denser regions in the south (e.g. 10th district) show higher temperatures compared to their surroundings.

The mean land surface temperature of the present scenario (i.e. 2020) evinces an increase of 0.4 K, resulting in 16.2 °C over the total area of Vienna. In comparison to the previous scenario, the mean surface temperature for every class has increased, showing an outcome of 12.7 °C on water bodies, 17.5 °C on the built-up areas, 15.2 °C on vegetated surfaces and 16.7 °C over low vegetated bare soil areas.

It can be obtained that the 2020 scenario shows a higher number of maximum temperature “hot spots” distributed over the city. Similarly, to the previous scenario, the eastern and western forest areas as well as the river area show the lowest temperature values.

As mentioned in chapter 3.5, the land surface temperature for the future scenario (i.e. 2055) was not computed from the respective classified land use/land cover map, but projected based on a linear statistical method.

The land surface temperature results are displayed in Figure 15.

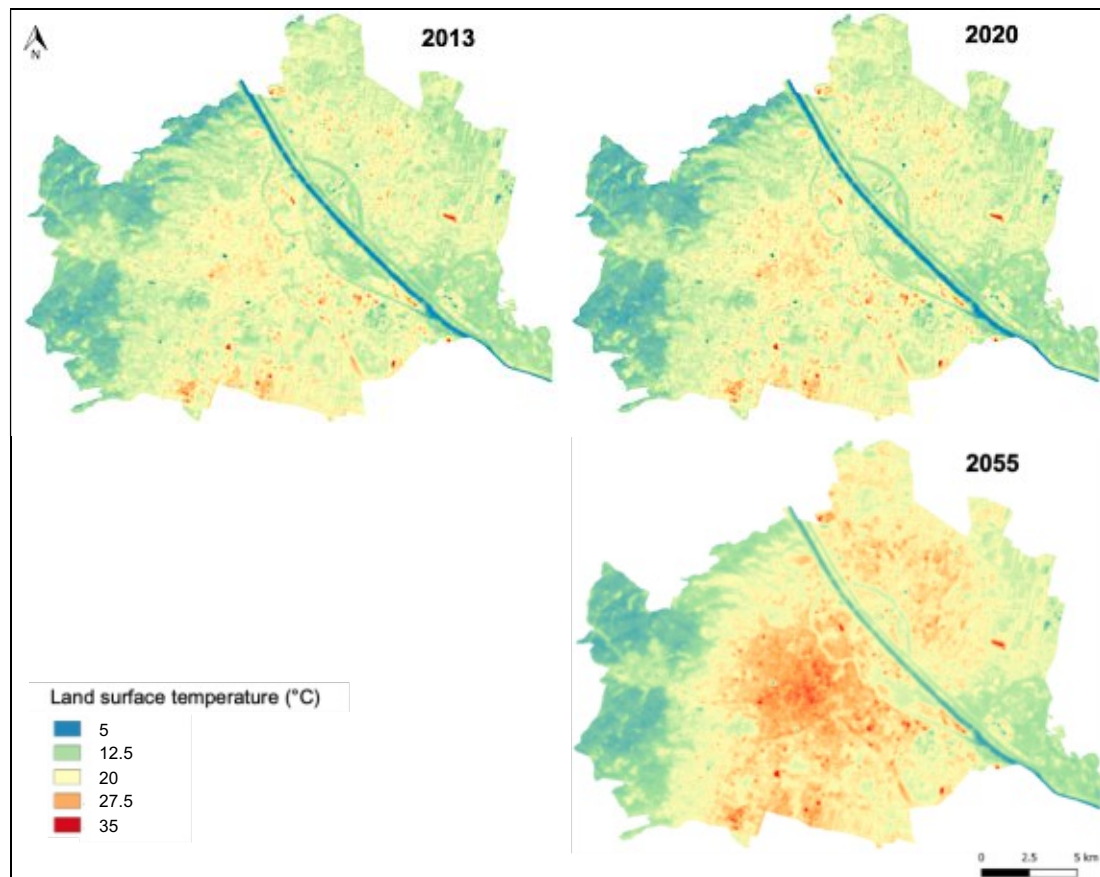


Figure 15: Land surface temperatures in Vienna (QGIS 2020)

The results indicate that the city center as well as the southern and north/north-eastern part experience significant increase in temperature over the course of the next 35 years. Not only the built-up areas evince temperature rise, but also the eastern and western forest and grassland regions face higher surface temperatures. It can be seen in the projected scenario, that the mean surface temperature of 18.0 °C indicates an increase of 1.8 K, compared to the present scenario of 2020.

By comparing the respective histograms of each scenario, it can be obtained that the development of the distribution is undergoing a shift in the positive x-direction: The highest frequencies were identified in the 17 °C to 18 °C range for the past condition, and in the 17.5 °C to 18.5 °C range for the present condition. Further, the highest frequencies for the 2055 scenario occur in the range of 18 °C to 21 °C.

The histograms of the land surface temperature results can be seen in Appendix 5.

Table 19: Mean zonal surface temperatures of the macro classes water, built-up, vegetation and bare soil, for past, present and future condition (°C) (QGIS 2021)

Mean zonal surface temperature (°C)			
Scenario	2013	2020	2055
Class			
Water	12.3	12.7	14.4
Built-up	17.2	17.5	19.9
Vegetation	14.7	15.2	16.4
Bare soil	16.7	16.5	18.1

Moreover, the frequency distribution of the three scenarios show two modes, respectively, significantly occurring around the 12 °C temperature mark. These peaks are likely to result from the temperature distribution of the water surfaces, which account for the lowest results. A zonal analysis of the mean surface temperatures for each macro class was computed in QGIS and is represented in Table 19.

5 CONCLUSION

5.1 Results evaluation

The classification result generated by MOLUSCE shows realistic values regarding the growing area of impervious surfaces. It appears to be plausible that bare soil areas, which in many cases are not only farmland but also unused and barren land are going to be used for constructing new buildings and roadwork. Moreover, the development of infrastructural connections such as roadwork public transport expansion may contribute to the densification of the city over time.

One reason for the increase in built-up area might be the densification of the urban space in the inner 15 districts of the city. According to the city's statistics, the years between 2013 and 2020 had a significantly higher rate of new constructions, resulting in densification of the city. Additionally, Vienna's population has grown by 3.95 % between the years 2013 and 2020 (Statistik Austria 2020).

Regarding the water surfaces, no significant changes between 2013 and 2020 could be seen. The surfaces covered with water were classified to be 3.7 % in 2013 as well as in 2020. With a percentage of 3.6 % in 2055, the area of water covered surfaces remained almost the same for the future scenario of 2055.

5.2 Statistical validation

Due to the presence of bad quality and cloud contaminated pixels (see 5.3), the LST outputs are subject to a plausibility check. The box plots generated for the respective scenario display the extreme values, upper and lower fence, first and third quartile, mean and median values as well as possible outliers. By considering upper and lower fences, outliers are cordoned off from the bulk data set, which allows for better understanding of the results. As to be seen in Appendix 6, the interquartile range (IQR) of both scenarios are 3.7 K and 3.9 K, respectively, while the IQR is shifted 0.25 K towards the positive x-direction from 2013 to 2020. The median of the present scenario is 0.4 K higher than median of the past scenario. Following this scheme, the mean values also differ approximately 0.4 K over the time of seven years. All outliers are extreme outliers, starting below the lower fence at 8.55 °C at minimum and above the upper fence at 23.27 °C (2013) and 23.98 °C (2020) at maximum. The lower fences do not show significant changes over time, while the upper fences result in a temperature difference of 0.7 K in the positive direction.

In comparison to the past and present scenarios, the box plot of the 2055 LST shows significantly higher characteristics. As to be seen in Figure 16, the IQR covers a difference of 4.8 K, defined by the first quartile at 15.57 °C and the third quartile at 20.40 °C. Mean and median values are 17.99 °C and 18.46 °C, respectively, which account for an increase of 1.78 K compared to the respective 2020 values. Moreover, the differences between the extreme outliers and the upper and lower fence are lower compared to the previous scenarios. While the upper fence increased by 3.7 K compared to 2020, the lower fence slightly decreased by 0.4 K.

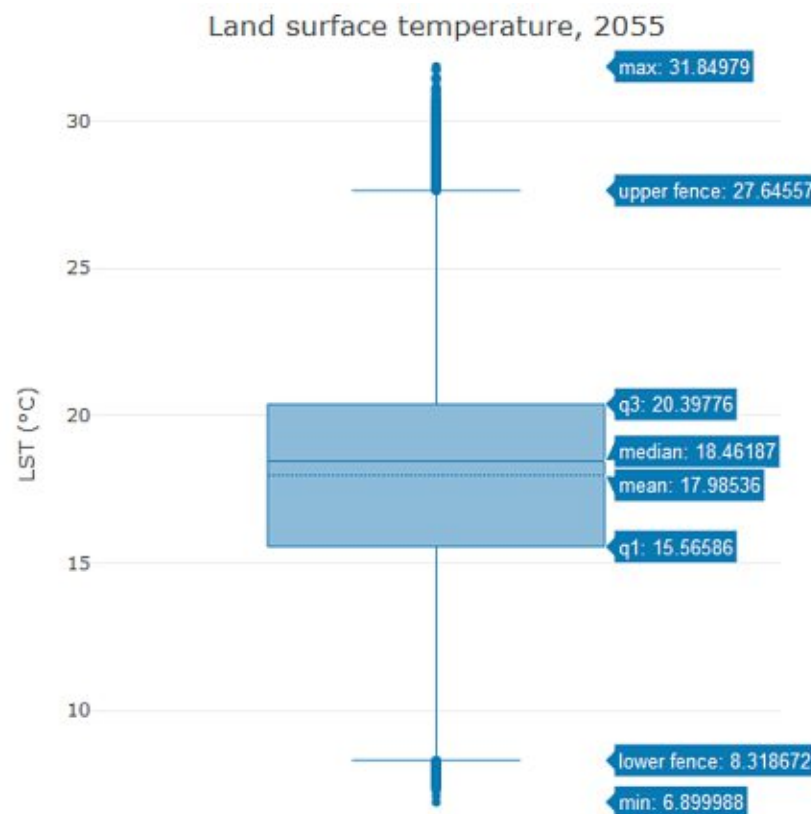


Figure 16: Box plots of the LST outputs of 2055 (QGIS 2021)

Comparing the box plots of the scenarios confirms the increasing trend of the LST outputs. By neglecting extreme outliers, in all likelihood caused by bad quality pixels, the performance and the tendency of the LST outputs can be assessed in a more plausible way. The box plots confirm the findings obtained under chapter 4.2.

Furthermore, as per the NOAA Global Climate Report, the annual surface temperature in Europe has increased at an average rate of 0.46 K per decade since 1981. This increase rate accounts for the three-fold of the increase rate until 1910, when it was 0.14 K per decade. The NOAA Global Climate Report trend – accounting for a 1.61 K trend per 35 years (i.e. from 2020 to 2055) – agrees with the findings of the study, which conclude a 1.78 K trend in the respective period under review (NOAA 2020).

5.3 USGS Landsat Collection 2 Temperature Product

In December 2020, USGS released Landsat Collection 2 Surface Temperature data via EarthExplorer. The tool provides surface temperature (in Kelvin) values and can be used for global energy balance studies, hydrologic modelling, monitoring crop and vegetation health, as well as extreme heat events caused by urban heat island effect or natural hazards such as volcanic eruptions and wildfires (USGS 2020).

As per USGS, the bands listed in (Figure 17) shall allow for displaying land surface temperatures in GIS software. The respective bands as well as all other bands available from Collection 2 Level 2 were downloaded and imported into QGIS in order to compare the results.

	Collection 2 Surface Temperature	Collection 1 Surface Temperature (on demand, U.S. ARD)
Fill Value	0	-9999
Scaling Factor	0.00341802 + 149.0	0.1
Data Type	Unsigned 16-bit integer	Signed 16-bit integer
Valid Range	1-65535	1500-3730
Atmospheric Reanalysis Source	GEOS-5 FP-IT (2000-present) MERRA-2 (1982-1999)	NARR
Quality Band	L1 QA_Pixel L1 QA_RADSAT L2 SR_QA_AEROSOL	Level-2 PIXELQA Level-2 RADSATQA Level-2 SRAEROSOLQA

Figure 17: Landsat Collection 2 surface temperature enhancements (USGS 2020)

According to USGS, Band 10 of the product can be used to derive surface temperature (ST) in degree Celsius following equation (19).

$$ST = Band10 * 0.00341802 + 149.0 - 273.15 \quad (19)$$

It has been found that the input bands were lacking 46,619 out of 414,086 (2013 scenario) and 46,489 out of 414,216 (2020 scenario) pixels, which accounts for about 11.2 % of not available data for each scenario. The extreme and mean values of both scenarios are summarized in Table 20.

Table 20: LST output values of the USGS Landsat 8 Collection 2 Level 2 surface temperature product (USGS 2021)

USGS L8 C2-L2	LST (°C)		
	Min.	Mean	Max.
2013	16.98	27.03	39.18
2020	17.17	26.01	38.53

It has been found that the two scenarios provided by the Landsat 8 Collection 2 Level 2 (L8-C2L2) surface temperature product show similar extreme and mean values, where the mean and maximum LST values of the 2020 scenario are even lower than the respective outputs of the past scenario. This might be due to the information gaps (i. e. missing pixels) in the districts 2, 11 and 20 to 23, predominantly affecting areas in the southern to south-eastern and the northern to north-eastern parts of the city (Figure 18).

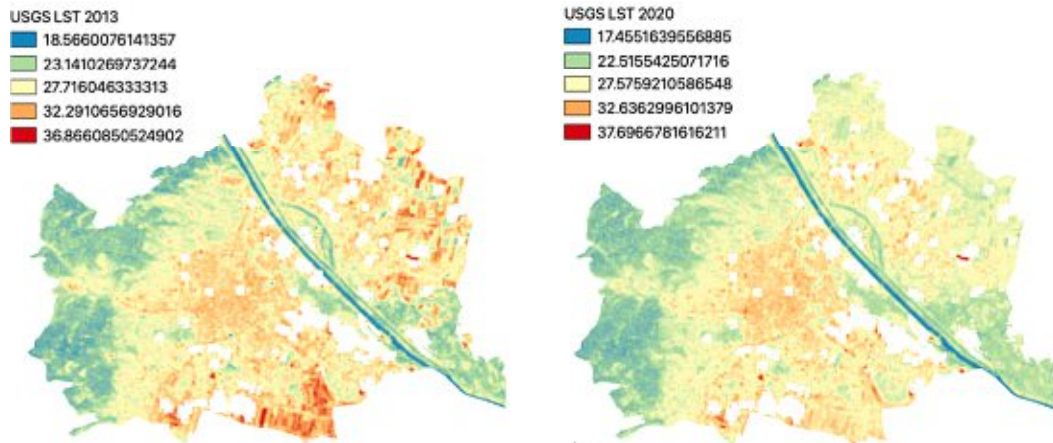


Figure 18: LST outputs of the Landsat 8 Collection 2 Level 2 surface temperature product: white areas represent missing data (USGS 2021)

Moreover, the two scenarios calculated with the L8-C2L2 product show multiple “hot spots”, mainly distributed over the north-eastern and south areas of the city (e.g. Figure 19). Since these areas are mostly covered with farmland, grassland and bare soil, the temperature distribution does not appear to reflect the real situation.

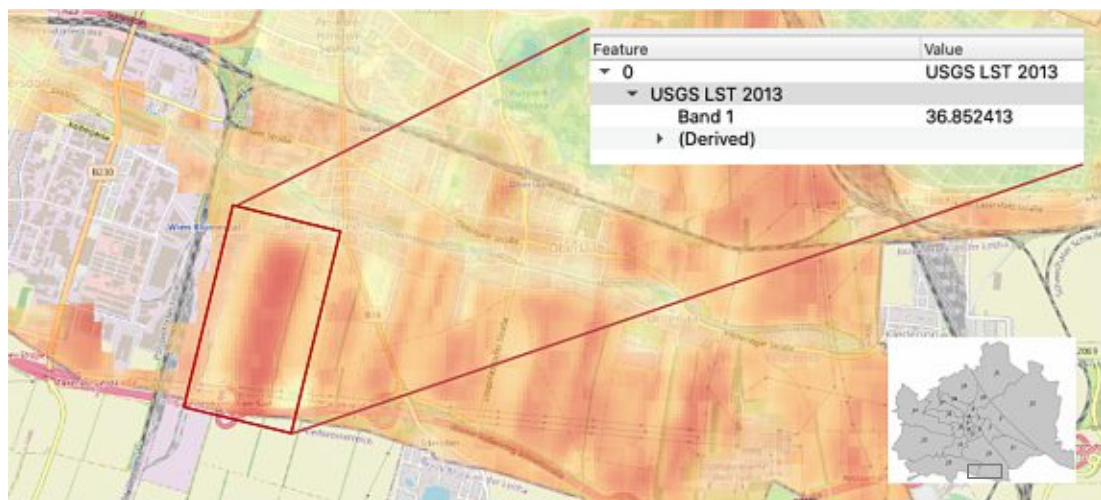


Figure 19: Bare soil areas in the south of the city, showing high LST values as per L8-C2L2 product (USGS 2021)

Furthermore, it was found that the areas with the lowest calculated LST outputs of the 2013 and 2020 scenario partially correspond to the missing pixel areas of the L8-

C2L2 product. As an example, the area surrounding the Stadthalle in the 15th district displayed the minimum values of 1.67 °C and 2.55 °C, respectively. In the L8-C2L2 product, this area does not have any pixels assigned to it (Figure 20).



Figure 20: Missing data at the Stadthalle (15th district) in the LST outputs of the L8-C2L2 product with OpenStreetMap underlying layer (USGS 2021)

As per USGS (2020), clouds and possible cloud shadows account for irregularities in the surface temperature retrievals. This error – traced back to the thermal calibration of the product – is well known. The ongoing efforts to mitigate this error is majorly focused on understanding the “ghosting issues” with Landsat 8.

According to Schott et al. (2014), the ghosting issues include differences e.g. in the calibration or spatial/temporal anomalies, leading to residual bias errors in band 10. Moreover, additional filters are being considered which may allow for small errors in the automated calibration, but remove pixels contaminated by clouds and cloud shadows.

5.4 Limitations

The results from this study are likely to be subject to a number of limitations which shall be explained in the following sections.

5.4.1 Data basis

Although the satellite images were collected within three days in the respective year and cloud coverage was below 1 %, the weather conditions might differ from another and therefore affect the footage. In general, the timing of the Landsat thematic mapper at satellite overpass in Vienna (11:45 a.m. CEST) is not ideal because the thermal bands tend to peak between midday and the early afternoon. Furthermore, the calculated near-surface air temperatures for the past and present scenario may include irregularities due to limited weather station data availability for the past scenario. Since the 2013 near-surface air temperature only considers two weather stations (Wien-Mariabrunn and Wien-City) while the 2020 scenario considers seven weather stations, this limited information may account for inaccuracies in the later stage of the LST calculation.

5.4.2 MOLUSCE

Moreover, it is possible that some inaccuracies occurred in the course of classifying the land use/land cover of the future condition. As an example, MOLUSCE predicted single classified water pixels evenly distributed over the study site, where in reality no water bodies could be identified. As an example, Figure 21 provides a comparison of the predicted land use/land cover classification by MOLUSCE, and the satellite overview from Google Maps. It can be seen, that the blue pixels that were classified as water surfaces are vegetated areas in the satellite image.



Figure 21: Classification inaccuracies by MOLUSCE compared to Google Maps (2021)

For further research it can be recommended to include more spatial variables in the process of the MOLUSCE classification in order to train the machine more accurately to the given scenario. The MOLUSCE classification accuracy is quantified by kappa

statistics. In order to generate a more accurate classification, it is recommended to target a kappa value approaching 1 (NextGIS 2014).

5.4.3 Image quality

Additionally, some bad quality pixels were proven to affect the results in a negative way. On closer examination of band 7 for 2013 and 2020 satellite imagery data, some pixels stand out in comparison to the whole image. For example, the Stadthalle (i.e. concert hall) in the 15th district has a high-reflective roof which might have affected the recording by the satellite. As to be displayed in Figure 22, band 7 of the Landsat 8 imagery past scenario, areas like these can be seen as striking white pixels.

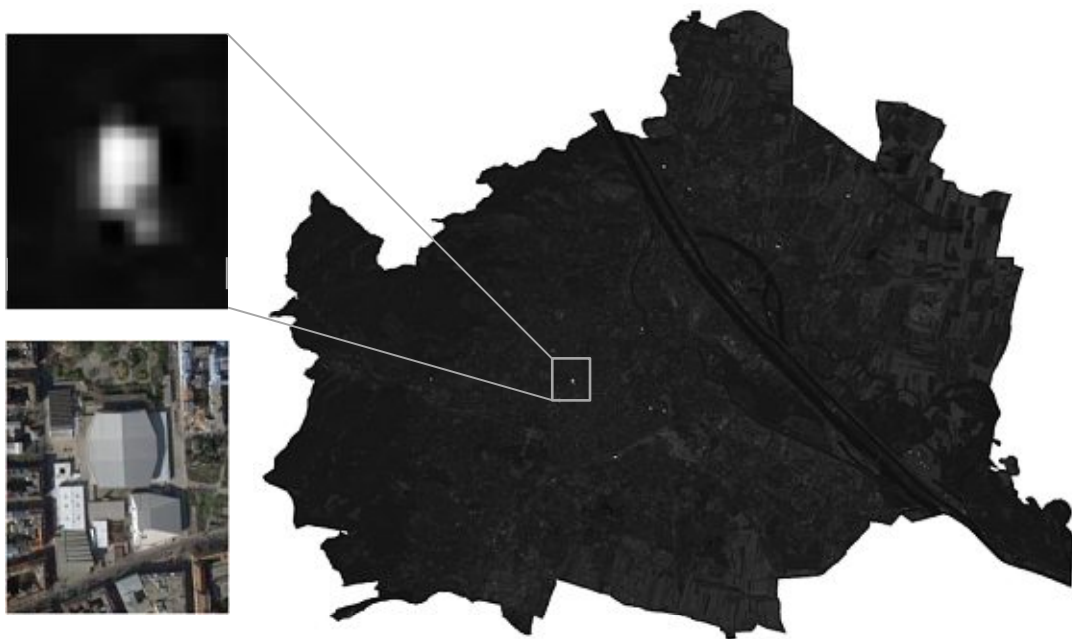


Figure 22: Satellite image of Stadthalle in the 15th district and Landsat 8, band 7, of the 2013 scenario (Google Maps 2021, QGIS 2021)

The area of white pixels is very likely to be responsible for causing the land surface temperature minima for past, present and future scenario, although the origin of the white pixels is not completely clear. In principle, Landsat 8 band 7 covers the shortwave infrared (SWIR 2), which are being used in order to distinguish between wet and dry earth (USGS 2017).

By overlaying OpenStreetMap, land cover classification maps and land surface temperature maps with 50 % transparency in QGIS, it can be seen that the three absolute minimum results of the land surface temperature calculations – being 1.67 °C, 2.55 °C and 6.90 °C, respectively - were calculated for the roof area of the Stadthalle (Figure 23).



Figure 23: Minimum land surface temperature occurrence in the three scenarios 2013, 2020 and 2055 (QGIS 2021)

5.5 Mitigation measures

5.5.1 Political strategies

Overall, urban areas are becoming more uncomfortable places to live due to higher temperatures during daytime and heat stagnation during nighttime. Higher temperatures boost demand for air conditioning and ventilation, which results in increased energy consumption.

In Geneva 1979, it was discussed that climate change required global counteracting measures, until in 1992, in Rio de Janeiro, the United Nations signed the frame agreement. The participating countries agreed on taking the responsibilities to reduce greenhouse gas emissions and tackle climate change. Since the catalogue of measures was not mandatory for the participating countries at that point in time, the agreement was manifest in the Kyoto Protocol in 1997, in which the reduction of greenhouse gases was made mandatory for industrial countries. In the first phase, the Kyoto Protocol includes six measures which had to be implemented for the years of 2008 to 2012. At the end of 2012, the second phase was added to the Kyoto Protocol, lasting until 2020. Unfortunately, only industrial countries agreed on the Kyoto Protocol, while the major contribution to greenhouse gases within the last decade derived from developing countries. Due to capitalist structures, most companies produce their goods in developing countries where fiscal expenditures are lower, and staff is cheaper. Overproduction, air, land and water pollution therefore

make developing countries the “main” contributors of greenhouse gas emissions. Whereas in reality, a total number of 100 companies is responsible for 71 % of the global greenhouse gas emissions since 1988 (Griffin 2017).

In December 2015, a new version of the Protocol was released: the Paris Agreement. The Paris Agreement marks a milestone in the course of combating climate change with regard to the following major goals:

- i. Limiting global climate change to a maximum of 2 °C compared to pre-industrial threshold values, including efforts in order to stay below 1.5 °C
- ii. Net-zero global greenhouse gas emissions by mid 21st century
- iii. Nationally Determined Contributions (NDC) presented and applied by all nations in order to reduce emissions
- iv. Adapting to inevitable climate change consequences with instant combating measures
- v. Supporting developing countries with financing, technology and capacity development

The first phase of the Kyoto Protocol was accomplished by the Austrian nation. Aside from inland measures, Austria bought credit notes from mitigation measures from other nations. In addition to the Kyoto Protocol’s second phase, the European Union released climate change target measures. (“EU Klima- und Energiepaket 2020”), resulting in an emission reduction of 16 % by 2020 compared to 2005. For the period until 2030, the European Union agreed on the implementation of additional goals regarding climate change (“EU Klima- und Energiepaket 2030”). This agreement includes an EU-wide goal in reducing greenhouse gas emission by at least 40 % by 2030, compared to 1990 (UNFCCC 2021).

5.5.2 Sustainable city development

Recently, a strong dependence on resilience as has been identified in order to cling to a more sustained future, which makes mitigating climate change inevitable for the future. It is necessary response to environmental hazards, how habitats and ecosystems can re-organize themselves after a disturbance, or how vulnerable a system is with regard to any probable disturbances. As per Mitchell, today’s sustainable strategies are expected to maintain the ability to deliver their intended benefits regardless of any possible future threats. According to Yamamoto, in the early 2000s, local governments began to make remarkable milestones in implementing systemic solutions so as to mitigate urban heat island effect. For

example, these approaches include the greening of urban spaces by mandating the promotion of greening and subsidizing the cost of it. Moreover, incentivizing rooftop greening by promising higher floor-area ratios of the building would be another example. As per Yamamoto, the application of these “sporadic measures” may be effective temporarily in terms of lowering urban temperatures, but they are not going to provide a lasting approach over the long term with regard to urban heat island effect. “It is imperative that regional mitigation measures have to be implemented simultaneously in order to achieve sustainable and lasting satisfactory results” (Yamamoto 2006).

Various studies have used a high number of tools and techniques including in situ measurement, monitoring as well as computational fluid dynamics (CFD) simulation in order to improve measurement, evaluation and prediction of the UHI effect. Regardless applications and approaches used, major assessment methods such as Leadership in Energy and Environmental Design (LEED) or Building Research Establishment Environmental Assessment Methodology (BREEAM) include strict criteria for UHI effect mitigation. Even though this number of criteria is not directly described as UHI mitigation actions, it can be directly associated with UHI effects. This is possible due to the target of improving the health and well-being of the environment by offering the benefits of mitigation of UHI effects. These are capable of informing and, in the most optimistic scenarios, influencing UHI mitigation strategies indirectly. Subsequently, it can be agreed on the following parameters across all the present and practiced techniques and strategies with regard to UHI effect mitigation:

- i. Ventilation of passages of air
- ii. Shading of buildings (trees, adjacencies, balconies etc.)
- iii. Greening of façades and roofs
- iv. Water use cooling
- v. Use of high albedo materials on buildings’ external surfaces

However, in order to appropriately select a UHI measure technology, the relationship between the environment where the tool shall be applied and the effect of introducing the respective technology must be studied. The application of sustainable strategies can be evaluated using the Urban Futures Assessment Method (UFAM) (Figure 24), which assesses the resilience of a selected mitigation strategy (Lombardi 2012).

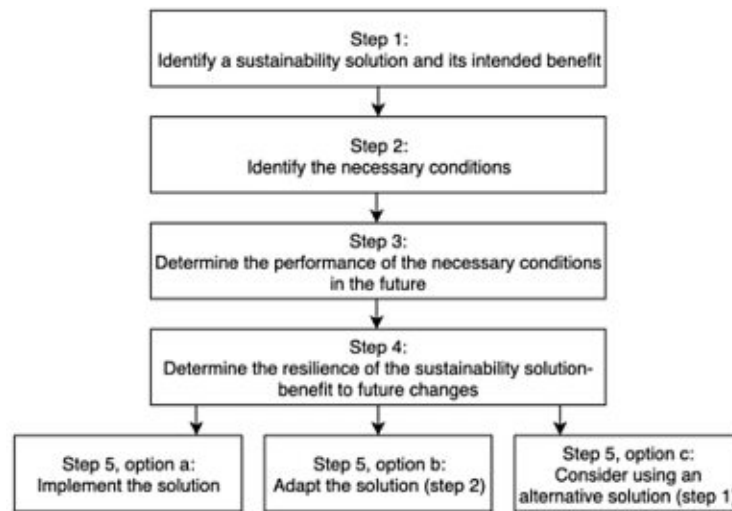


Figure 24: Urban Futures Assessment Method (Lombardi 2012)

5.5.3 Challenges

The IPCC published four alternative scenarios, the Representative Concentration Pathways (RCP) which try to represent a range of possible future emissions. The scenarios include one business-as-usual scenario (RCP2.6), two medium stabilization scenarios (RCP4.5 and RCP6.0) and one very high baseline emission scenario (RCP8.5). In contrast to that, recent studies found that, surprisingly, the business-as-usual baseline is not moving towards RCP2.6, but rather towards RCP8.5, commonly known as the “worst-case scenario” (Schwalm et al. 2017).

Figure 25 represents the RCP scenarios with regard to global surface temperature change. Inserting the result for the mean surface temperature anomaly change between 2020 and 2055 (see chapter 4.2), namely 1.8 K, the intercept at 2055 can be recorded in the RCP8.5 scenario.

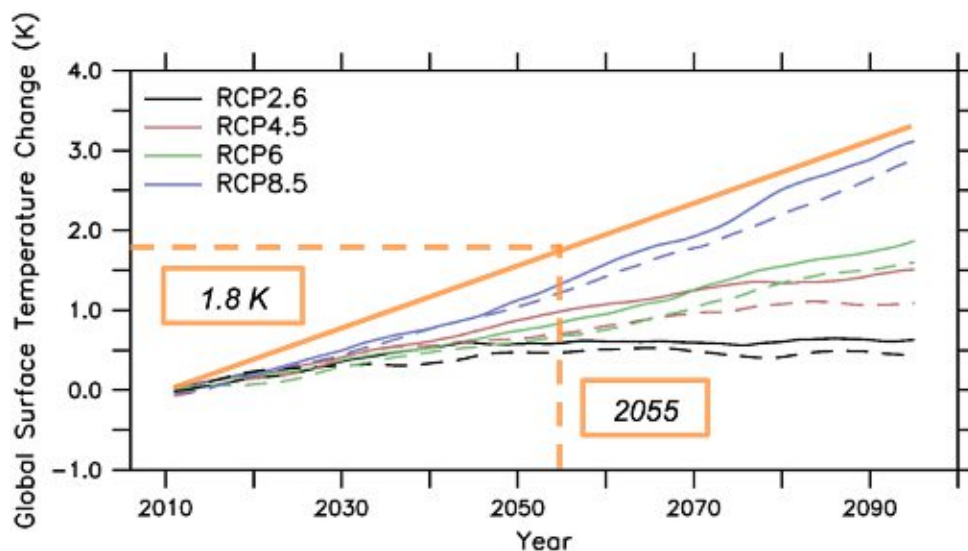


Figure 25: RCP scenarios of global surface temperature change (modified) (IPCC 2018)

6 DISCUSSION

This study is conducted in several different steps. The final goal was to define the basic parameters that affect urban microclimate and to elaborate an approach to predict land use/land cover change and surface temperature maps based on satellite imagery. The hypothesis that GIS software can be used in order generate such predictive maps can be confirmed. It can be seen that engaging satellite data provides an accessible approach to predict future development in urban settings. The elaborated approach is not limited to the specific study area Vienna, Austria, but can be applied to any setting on the urban scale, given the required satellite imagery is publicly available. For the effectiveness of this methodology, further analysis can be helpful to fully represent the climatic behavior of further points in time. This might include diurnal and seasonal variability in data acquisition.

In general, change in land use and land cover mainly caused by urbanization boost last surface temperature and therefore urban heat island effect. Additionally, vegetated areas like parks and increased greenery in an urban setting could contribute to improving microclimate and balance land surface temperature, just as the role of water bodies like rivers and lakes. Vegetated areas and water bodies could also separate urban thermal fields, reducing thermal radiation and decelerating UHI effect. The sealed surfaces and the building mass are the main sources in LULC to boost urban temperatures in Vienna, Austria. Therefore, building planning and density along vegetated areas will directly influence the development of urban microclimate. Moreover, the densification of urban space can have a crucial effect on UHI: building upward with limited horizontal width provides shade, which has a cooling effect for adjacent buildings, and, additionally, saves (unsealed) land.

Regarding the future development, research has shown that sustainable mitigation strategies are inevitable for a positive long-term change in order to combat climate change. The results prove that there is a current trend that approaches the worst-case scenario, RCP8.5. The consequences of the steady increase in temperature might lead to a loss of biodiversity, ecological system collapse and environmental threats and hazards. Cities must, on one hand, be designed to withstand such disturbances and be resilient in order to sustain. Simultaneously, greenhouse gas emissions must be reduced drastically in order to mitigate the current increase not only in temperature but also in other driving forces such as volatile organic compounds (VOCs) and CO₂.

7 INDEX

7.1 List of abbreviations

°C	<i>Degree Celsius</i>	L8-C2L2	<i>Landsat 8 Collection 2 Level 2</i>
A	<i>Air density</i>	Lat	<i>Latitude</i>
A_i	<i>Radiance rescaling factor (additive)</i>	LEED	<i>Leadership in Energy and Environmental Design</i>
ANN	<i>Artificial Neural Network</i>	Lon	<i>Longitude</i>
AR	<i>Aspect ratio</i>	LST	<i>Land surface temperature</i>
BREEAM	<i>Building Research Establishment Environmental Assessment Methodology</i>	LULC	<i>Land use/land cover</i>
c	<i>Heat capacity</i>	m	<i>Meter</i>
C	<i>Class</i>	MB	<i>Mariabrunn</i>
CEST	<i>Central European Summer Time</i>	MC	<i>Macro class</i>
CFD	<i>Computational fluid dynamics</i>	M_i	<i>Radiance rescaling factor (multiplicative)</i>
CO ₂	<i>Carbon dioxide</i>	mm	<i>Millimeter</i>
DF	<i>Donaufeld</i>	MOLUSCE	<i>Models for Land Use Change Evaluation</i>
DOS	<i>Dark object subtraction</i>	MTL	<i>Material template library</i>
$d\epsilon$	<i>Effect of the geometrical distribution of the natural surface and internal reflections</i>	MWA	<i>Mono-window algorithm</i>
E	<i>Saturation mix ratio of water vapor and air</i>	NASA	<i>National Aeronautics and Space Administration</i>
EERE	<i>Energy Efficiency and Renewable Energy</i>	NATO	<i>North Atlantic Treaty Organisation</i>
EPSG	<i>European Petroleum Survey Group Geodesy</i>	NDC	<i>Nationally Determined Contributions</i>
F	<i>Geometrical shape factor</i>	NDVI	<i>Normalized Difference Vegetation Index</i>
GD	<i>Großenzersdorf</i>	NOAA	<i>National Oceanic and Atmospheric Administration</i>
GIS	<i>Geographical information systems</i>	OLI	<i>Operational Land Imager</i>
GPS	<i>Global positioning system</i>	Pv	<i>Proportion of vegetation</i>
ha	<i>hectare</i>	Q_{cal}	<i>Quantized and calibrated standard product pixel value</i>
HW	<i>Hohe Warte</i>	QGIS	<i>Software name (formerly "QuantumGIS")</i>
IPCC	<i>Intergovernmental Panel on Climate Change</i>	RCP	<i>Representative Concentration Pathways</i>
IQR	<i>Inter-quartile range</i>	RMSE	<i>Root-mean-square deviation</i>
K	<i>Kelvin</i>	ROI	<i>Region of interest</i>
K_1	<i>Thermal conversion constant 1</i>		
K_2	<i>Thermal conversion constant 2</i>		
km	<i>kilometer</i>		
L_λ	<i>Spectral radiance</i>		

RT.....	<i>Real Time</i>	t_{Tmax}	<i>Number of hours between local solar noon and the time of Tmax</i>
Rw ₀	<i>Ratio of water vapor content at the first layer to the total</i>	UFAM.....	<i>Urban Futures Assessment Method</i>
SCP.....	<i>Semi-Automated Classification Plugin</i>	UHI.....	<i>Urban Heat Island</i>
ST.....	<i>Surface temperature</i>	UI.....	<i>Urbanization Index</i>
SW.....	<i>Schwechat</i>	UL.....	<i>Unterlaa</i>
t.....	<i>Time at satellite overpass</i>	US EPA.....	<i>United States Environmental Protection Agency</i>
T.....	<i>Temperature</i>	USGS.....	<i>2</i>
T ₀	<i>Near-surface air temperature</i>	VOC.....	<i>Volatile organic compound</i>
T ₁₀	<i>Brightness temperature</i>	w.....	<i>Water vapor content</i>
T _a	<i>Effective mean atmospheric temperature</i>	w ₀	<i>Water vapor content at the ground of the atmosphere</i>
t _{dl}	<i>Day length</i>	WoE.....	<i>Weight of Evidence</i>
TIRS.....	<i>Thermal Infrared Sensor</i>	WRS.....	<i>World Reference System</i>
T _{max}	<i>Daily maximum near-surface air temperature</i>	Z _u	<i>Urban zone</i>
T _{min}	<i>Daily minimum near-surface air temperature</i>	ε.....	<i>Emissivity</i>
TOA.....	<i>Top of atmosphere</i>	ε _s	<i>Emissivity (soil)</i>
		ε _v	<i>Emissivity (vegetated)</i>
		λ.....	<i>Thermal conductivity</i>
		μm.....	<i>Micrometer</i>

7.2 List of figures

Figure 1: Share of the world population living in urban areas, 2050 (Global Change Data Lab, 2020).....	1
Figure 2: Natural cooling effect of a tree	10
Figure 3: Incident solar radiation in rural areas and urban canyon effect (TERI, 2017)	12
Figure 4: Location of the study area Vienna, Austria (QGIS, 2020).....	15
Figure 5: Dimensions of Landsat 8 images at WRS-2 190-026 (Earth Explorer, 2020)	16
Figure 6: DOS1 Correction by SCP (Congedo, 2020).....	22
Figure 7: Macro classes and classes for the training input in SCP (Congedo, 2020)	23
Figure 8: Region growin algorithm (Congedo, 2020)	23
Figure 9: Spatial variable map of Vienna: distance to district center (QGIS, 2020) .	24
Figure 10: Modified Mono-window Algorithm with additional input parameters (T_{10} and T_a) (Wang, et al., 2019)	27
Figure 11: Spatial interpolation for T_0 in 2013 (QGIS, 2020).....	29
Figure 12: Spatial interpolation for T_0 in 2020 (QGIS, 2020).....	29
Figure 13: LULC classification of Vienna (QGIS, 2020)	35
Figure 14: Change of land use/land cover area over time, including trendlines.....	36
Figure 15: Land surface temperatures in Vienna (QGIS, 2020).....	38
Figure 16: Box plots of the LST outputs of 2055 (QGIS 2021).....	41
Figure 17: Landsat Collection 2 surface temperature enhancements (USGS, 2020)	42
Figure 18: LST outputs of the Landsat 8 Collection 2 Level 2 surface temperature product: white areas represent missing data (USGS 2021)	43
Figure 19: Bare soil areas in the south of the city, showing high LST values as per L8-C2L2 product (USGS 2021)	43
Figure 20: Missing data at the Stadthalle (15th district) in the LST outputs of the L8-C2L2 product with OpenStreetMap underlying layer (USGS 2021)	44
Figure 21: Classification inaccuracies by MOLUSCE compared to Google Maps (2021)	45
Figure 22: Satellite image of Stadthalle in the 15th district and Landsat 8, band 7, of the 2013 scenario (Google Maps, QGIS 2021).....	46

Figure 23: Minimum land surface temperature occurrence in the three scenarios 2013, 2020 and 2055 (QGIS, 2021)	47
Figure 24: Urban Futures Assessment Method (Lombardi, 2012)	50
Figure 25: RCP scenarios of global surface temperature change (modified) (IPCC, 2018)	50

7.3 List of tables

Table 1: Typical albedo (Kotak, et al., 2015) and emissivity (Mohamed, et al., 2017) values for different surface types	8
Table 2: Heat capacity and thermal conductivity values for different materials (Greenspec, 2021)	9
Table 3: Evaluation matrix for the selection of the data set for the past condition (Point scale: Good = 2 pt, OK = 1 pt, bad = 0 pt)	17
Table 4: Evaluation matrix for the selection of the data set for the present condition (Point scale: Good = 2 pt, OK = 1 pt, bad = 0 pt)	18
Table 5: Landsat product identification (USGS, 2020).....	19
Table 6: Overview of the used satellite data from Landsat 8 (USGS, 2020).....	20
Table 7: Search parameters for Landsat 8 download in SCP (QGIS, 2020).....	21
Table 8: Center wavelength for Landsat 8 bands B2-B7 (QGIS, 2020)	22
Table 9: NDVI threshold method (Sobrino et al. 2001)	26
Table 10: a ₁₀ and b ₁₀ input parameters depending on the temperature range (Wang, et al., 2015)	27
Table 11: Relationship between T ₀ and T _a depending on the region (Wang, et al., 2015)	28
Table 12: Input parameters for near-surface air temperature (Qin, et al., 2001).....	28
Table 13: Relevant weather stations for the study (Kachelmann, 2020).....	29
Table 14: Radiance rescaling factors and band-specific thermal conversion constants (Congedo, 2020)	30
Table 15: Water vapor content and transmittance estimation equation (Wang, et al., 2015)	30
Table 16: E and A input parameters depending on air temperature (Wang, et al., 2015)	31
Table 17: Summary of the land use/land cover classification of past, present and future scenarios (in hectare and percent).....	34
Table 18: Summary of the land surface temperatures of 2013, 2020 and 2055	37
Table 19: Mean zonal surface temperatures of the macro classes water, built-up, vegetation and bare soil, for past, present and future condition (°C) (QGIS 2021)..	39
Table 20: LST output values of the USGS Landsat 8 Collection 2 Level 2 surface temperature product (USGS 2021)	42

7.4 List of equations

(1).....	4
(2).....	25
(3).....	26
(4).....	26
(5).....	26
(6).....	26
(7).....	26
(8).....	26
(9).....	27
(10).....	27
(11).....	28
(12).....	28
(13).....	28
(14).....	30
(15).....	30
(16).....	31
(17).....	31
(18).....	32
(19).....	42

8 LITERATURE

- Ackermann, B. (1985). Temporal march of the Chicago heat island. *Climate Appl. Meteor*(1), 547-554.
- Alves, E., & Lopes, A. (2017). The Urban Heat Island Effect and the Role of Vegetation to Address the Negative Impacts of Local Climate Changes in a Small Brazilian City. *Atmosphere*, 8(18), 1-14.
- Bueno de Morias, M., Guerrero, V., Dias de Freitas, E., Marciotto, E., Valdés, H., Correa, C., & Vera-Puerto, I. (2019). Sensitivity of Radiative and Thermal Properties of Building Material in the Urban Atmosphere. *Sustainability*, 11(6865).
- Cain, F. (2009). *Albedo Effect*. Retrieved August 2020, from <https://www.universetoday.com/39937/albedo-effect/>
- Camilloni, I., & Barrucand, M. (2012). Temporal variability of the Buenos Aires, Argentina, urban heat island. *Theoretical and Applied Climatology*(107), 47-58.
- Christen, A., & Vogt, R. (2004). Energy and Radiation Balance of a Central European City. *International Journal of Climatology*, 24(11), 1395-1421.
- Colunga, M., Cambrón-Sandoval, V., Suzán-Azpiri, H., Guevara-Escobar, A., & Luna-Soria, H. (2015). The role of urban vegetation in temperature and heat island effects in Querétaro city, Mexico. *Atmósfera*, 28(3), 205-218.
- Congedo, L. (2020). *Semi-Automatic Classification Plugin Documentation*. Retrieved January 2021, from <https://readthedocs.org/projects/semiautomaticclassificationmanual/downloads/pdf/latest/>
- Earth, B. (2021). *Climate Data Guide*. Retrieved January 2021, from <https://climatedataguide.ucar.edu/climate-data/global-surface-temperatures-best-berkeley-earth-surface-temperatures>
- EERE. (2013). *Solar Radiation Basics*. Retrieved September 2020, from <https://www.energy.gov/eere/solar/solar-radiation-basics>
- EPA. (2008). *Reducing Urban Heat Islands: Compendium of Strategies*. Retrieved August 2020, from <https://coolrooftoolkit.org/knowledgebase/reducing-urban-heat-islands-compendium-of-strategies-full/>

- EPA. (2017). *Reducing Urban Heat Islands: Compendium of Strategies*. Retrieved August 2020, from <https://www.epa.gov/sites/production/files/2014-06/documents/basicscompendium.pdf>
- EPA, U. (2017). *Causes of Climate Change*. Retrieved September 2020, from <https://archive.epa.gov/epa/climate-change-science/causes-climate-change.html#Greenhouse>
- EPSG. (2007). *EPSG:4326*. Retrieved August 2020, from <https://epsg.io/4326>
- Estes Jr., M. (2007). Urban Heat Islands. In M. King, C. Parkinson, R. Williams, & K. Partington (Hrsg.), *Our Changing Planet* (S. 179-181). Cambridge: Cambridge University Press.
- European Commission. (2020). *Paris Agreement*. Retrieved October 2020, from https://ec.europa.eu/clima/policies/international/negotiations/paris_en
- Favretto, A. (2018). Urban Heat Island analysis with Remote Sensing and GIS methods: an application in the Trieste area (North-East of Italy). *Bollettino della Società Geografica Italiana*, 14(1), 215-229.
- Fridays For Future. (2020). *Wir sind Fridays For Future*. Retrieved October 2020, from <https://fridaysforfuture.de/>
- Ganbar, G., Han, J.-Y., Ryu, Y.-H., & Baik, J.-J. (1998). Characteristics of the Urban Heat Island in a High-Altitude Metropolitan City, Ulaanbaatar, Mongolia. *Asia-Pacific J. Atmos. Sci.*, 49(4), 535-541.
- Global Change Data Lab. (2020). *Our World in Data*. Retrieved August 2020, from <https://ourworldindata.org/grapher/urban-population-share-2050>
- Greenspec. (2021). *Thermal mass*. Retrieved January 2021, from <https://www.greenspec.co.uk/building-design/thermal-mass/>
- Griffin, P. (2017). *The Carbon Majors Database - CDP Carbon Majors Report 2017*. CDP.
- IPCC. (2018). *Global Warming of 1.5 °C. An IPCC Special Report on the impacts of global warming of 1.5 °C above pre-industrial levels and related global greenhouse gas emission pathways, in the context of strengthening the global response to the threat of climate change*. IPCC.
- Kachelmann, J. (2020). *Kachelmannwetter*. Retrieved December 2020, from <https://kachelmannwetter.com>

- Khan, M., Ullah, S., Sun, T., Rehmann, A., & Chen, L. (2020). Land-Use/Land-Cover Changes and Its Contribution to Urban Heat Island: A Case Study of Islamabad, Pakistan. *Sustainability*, 12(3861).
- Kotak, Y., Gul, M., Muneer, T., & Ivanova, S. (2015). Investigating the Impact of Ground Albedo on the Performance of PV Systems. *7th International Conference on Solar Radiation and Daylight SOLARIS 2015*. Celje, Slovenia.
- Lombardi, D. (2012). *Designing resilient cities, A guide to good practice*. Bracknell: HIS BRE Press.
- Memon, R., Leung, D., & Liu, C.-H. (2010). Effects of building aspect ratio and wind speed on air temperature in urban-like street canyons. *Building and Environment*(45), 176-188.
- Mohamed, A., Odindi, J., & Mutanga, O. (2017). Land surface temperature and emissivity estimation for Urban Heat Island assessment using medium- and low-resolution space-borne sensors: A review. *Geocarto International*, 32(4), 455-470. Abgerufen am September 2020 von http://www-eng.lbl.gov/~dw/projects/DW4229_LHC_detector_analysis/calculations/emissivity2.pdf
- Mohr, M. (2020). *Die größten Städte in Österreich am 1. Januar 2020*. Retrieved September 2020, from <https://de.statista.com/statistik/daten/studie/217757/umfrage/groesste-staedte-in-oesterreich/#:~:text=%E2%80%99EST%C3%A4dte%E2%80%9C%20werden%20je%20nach%20Land,als%2010.000%20Einwohnern%20als%20St%C3%A4dte.>
- Morris, C., Simmonds, I., & Plummer, N. (2001). Quantification of the Influences of Wind and Cloud on the Nocturnal Urban Heat Island of a Large City. *Journal of Applied Meteorology*, 40(2), 169-182.
- NextGIS. (2014). *Molusce*. Retrieved October 2020, from <https://github.com/nextgis/molusce>
- NOAA. (2020, January). *State of the Climate: Global Climate Report for Annual 2019*. Retrieved 2021, from <https://www.ncdc.noaa.gov/sotc/global/201913>
- NOAA. (2020). *What's the Difference Between Weather and Climate?* Retrieved August 2020, from <https://www.ncei.noaa.gov/news/weather-vs-climate>

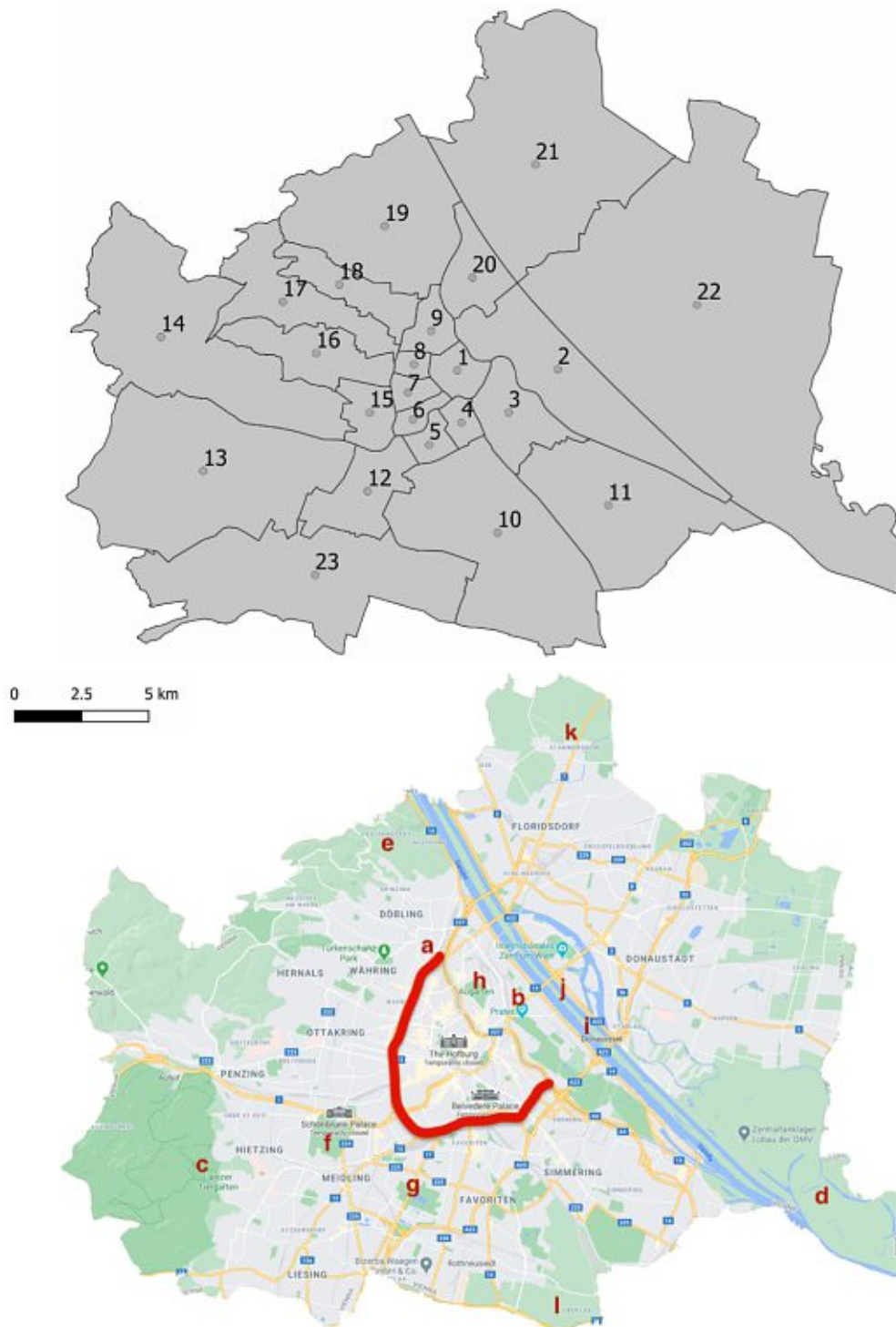
- QGIS. (2016). *QGIS User Guide*. Retrieved October 2020, from https://docs.qgis.org/2.18/en/docs/user_manual/preamble/preamble.html
- QGIS. (2020). *QGIS - The Leading Open Source Desktop GIS*. Retrieved August 2020, from <https://qgis.org/en/site/about/index.html>
- Qin, Z., Karniel, A., & Berliner, P. (2001). A mono-window algorithm for retrieving land surface temperature from Landsat TM data and its application to the Israel-Egypt border region. *Int. J. Remote Sensing*, 22(18), 3719-3746.
- Ritchie, H. (2018, January). *OurWorldInData*. Retrieved January 2021, from <https://ourworldindata.org/urbanization>
- Schott, R., Gerace, A., Raqueno, N., Ientilucci, E., Raqueno, R., & Lunsford, A. (2014). Chasing the TIRS ghosts: calibrating the Landsat 8 thermal bands. *Earth Observing Systems XIX*(92181A).
- Schwalm, C., Glendon, S., & Duffy, P. (2017). RCP8.5 tracks cumulative CO2 emissions. *Proceedings of the National Academy of Sciences*, 117(33), 19656-19657.
- Sobrino, J. (1989). Desarrollo de un modelo teórico para implementar la medida de la temperatura realizada mediante teledetección. Aplicación a un campo de naranjos. PhD dissertation. Valencia, Spain.
- Sobrino, J., Raissouni, N., & Zhou-Liang, L. (2001). A Comparative Study of Land Surface Emissivity Retrieval from NOAA Data. *Remote Sensing of Environment*, 75(2), 256-266.
- Statistik Austria. (2020). *Bevölkerung von Wien von 2010 bis 2020*. Retrieved August 2020, from <https://de.statista.com/statistik/daten/studie/317867/umfrage/prognose-zur-bevoelkerungsentwicklung-in-wien/#professional>
- Stewart, I., & Oke, T. (2012). Local climate zones for urban temperature studies. *Bull. Am. Meteorol. Soc.*(93), 1897-1900.
- Sundara Kumar, K., Udaya Bhaskar, P., & Padmakumari, K. (2012). Estimation of land surface temperature to study urban heat island effect using Landsat ETM+ Image. *International Journal of Engineering Science and Technology*, 4(2), 771-778.
- Taxacher, I., & Lehart, G. (2016). *Wien - Bezirke im Fokus. Statistiken und Kennzahlen*. Retrieved August 2020, from <https://www.wien.gv.at/statistik/pdf/bezirke-im-fokus-1-23.pdf>

- TERI. (2017). *Final Report on Urban Planning Characteristics to Mitigate Climate Change in Context of Urban Heat Island Effect*. Bangalore: The Energy and Resources Institute.
- Time and Date AS. (2021). *Wetter in Wien, Wien, Österreich*. Retrieved December 2020, from <https://www.timeanddate.de/wetter/oesterreich/wien>
- UNFCCC. (2021). *What is the United Nations Framework Convention Climate Change?* Retrieved January 2021, from <https://unfccc.int/process-and-meetings/the-convention/what-is-the-united-nations-framework-convention-on-climate-change>
- USGS. (2017). *Landsat Collections - What are Tiers?* Sioux Falls, SD, US: USGS EROS Center.
- USGS. (2020). *Landsat Collection 2*. Retrieved January 2021, from <https://www.usgs.gov/core-science-systems/nli/landsat/landsat-collection-2-level-2-science-products#:~:text=Landsat%20Level%2D2%20science%20products,generate%20a%20scientifically%20viable%20product>.
- USGS. (2020). *Landsat Collection 2 Level-2 Science Products*. Retrieved 2021, from <https://www.usgs.gov/core-science-systems/nli/landsat/landsat-collection-2-level-2-science-products>
- USGS. (2020). *Landsat Science*. Retrieved August 2020, from <https://landsat.gsfc.nasa.gov/>
- Wang, F., Qin, Z., Song, C., Tu, L., Karnieli, A., & Zhao, S. (2015). An Improved Mono-Window Algorithm for Land Surface Temperature Retrieval from Landsat 8 Thermal Infrared Sensor Data. *Remote Sensing*, 7, 4268-4289.
- Wang, L., Lu, Y., & Yao, Y. (2019). Comparison of Three Algorithms for the Retrieval of Land Surface Temperature from Landsat 8 Images. *Sensors*, 22(5049).
- Wonorahardjo, S., Sutjahja, I., Mardiyati, Y., Andoni, H., Thomas, D., Achsani, R., & Steven, S. (2020). Characterising thermal behaviour of buildings and its effect on urban heat island in tropical areas. *International Journal of Energy and Environmental Engineering*(11), 129-142.
- Yale University. (1997). *Department of Statistics and Science*. Retrieved 2021, from <https://statistics.yale.edu/>
- Yamamoto, Y. (2006). Measures to Mitigate Urban Heat Islands. *Sci. Tech. Trends.*, 18(1), 65-83.

- Yang, C., He, X., Yan, F., Yu, L., Bu, K., Yang, J., . . . Zhang, S. (2017). Mapping the Influence of Land Use/Land Cover Changes on the Urban Heat Island Effect - A Case Study of Changchun, China. *Sustainability*, 9(312).
- Yang, L., Qian, F., Song, D.-X., & Zheng, K.-J. (2016). Research on Urban Heat-island Effect. *Procedia Engineering*(169), 11-18.
- Yu, Z., Yao, Y., Yang, G., Wang, X., & Vejre, H. (2019). Strong contribution of rapid urbanization and urban agglomeration development to regional thermal environment dynamics and evolution. *Forest Ecology and Management*(446), 214-225.
- Zou, K.-H., Tuncali, K., & Silverman, S.-G. (2003). Correlation and simple linear regression. *Radiology*, 227(3), 617-22.

9 APPENDIX

Appendix 1: Maps of Vienna (districts and significant locations)



Appendix 1: Vienna districts map (QGIS 2020) and crucial locations regarding LULC classification (a: Gürtel, b: Prater, c: Lainzer Tiergarten, d: Lobau, e: Heiligenstadt, f: Schönbrunn, g: Wienerberg, h: Augarten, i: Donauinsel, j: Neue Donau, k: Stammersdorf, l: Oberlaa) (Google Maps 2021)

Appendix 2: Weather station observation data

		Weather station observation data								
Year		2013		2020						
Hour	Weather station	HW	SW	MB	City	HW	DF	UL	SW	GD
	0	N/A	15	11	16	14	14	15	15	13
1	N/A	14	11	16	13	13	14	12	13	
2	14	15	10	15	13	13	14	12	12	
3	N/A	14	10	15	12	13	13	12	12	
4	N/A	13	9	14	12	12	12	11	12	
5	13	12	9	14	11	12	12	10	11	
6	N/A	12	9	13	11	12	11	11	11	
7	N/A	14	9	13	11	11	12	11	10	
8	14	16	11	16	13	14	14	12	12	
9	N/A	17	15	17	16	17	15	15	15	
10	N/A	18	19	18	17	18	17	18	18	
11	20	20	20	19	19	20	20	19	19	
12	N/A	21	21	21	21	22	21	21	21	
13	N/A	23	22	23	22	23	22	22	23	
14	24	24	24	24	24	24	24	24	24	
15	N/A	25	25	25	25	25	25	25	25	
16	N/A	25	25	27	26	26	26	25	26	
17	24	25	26	26	26	26	26	25	26	
18	N/A	25	25	26	25	26	25	25	25	
19	N/A	24	22	25	23	24	24	23	24	
20	22	21	18	24	21	23	21	21	21	
21	N/A	19	16	23	19	20	20	18	19	
22	N/A	19	15	21	18	19	19	17	18	
23	19	19	15	19	17	17	18	18	16	
Min	13	12	9	13	11	11	11	10	10	
Max	24	25	26	27	26	26	26	25	26	
T ₀	20.51	20.29	20.60	23.26	22.00	22.00	21.24	20.24	20.92	

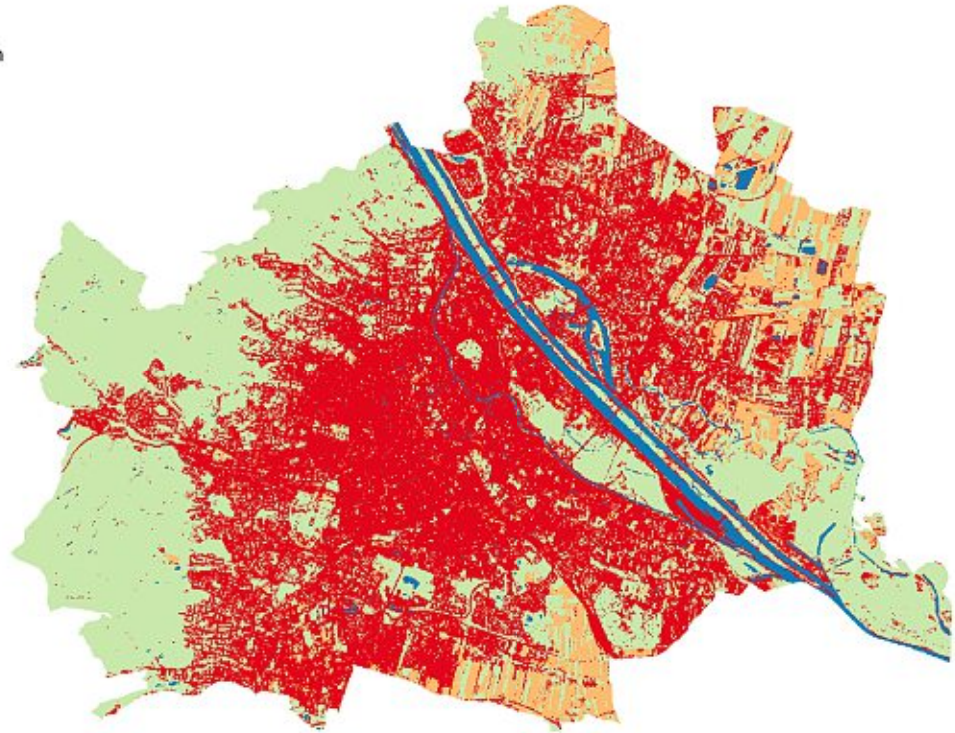
Appendix 2: Weather station observation data for the calculation of near-surface air temperature T_0 (Kachelmann, 2020)

Appendix 3: Land use/land cover change maps

Land use/land cover classification

LULC classes (2013)

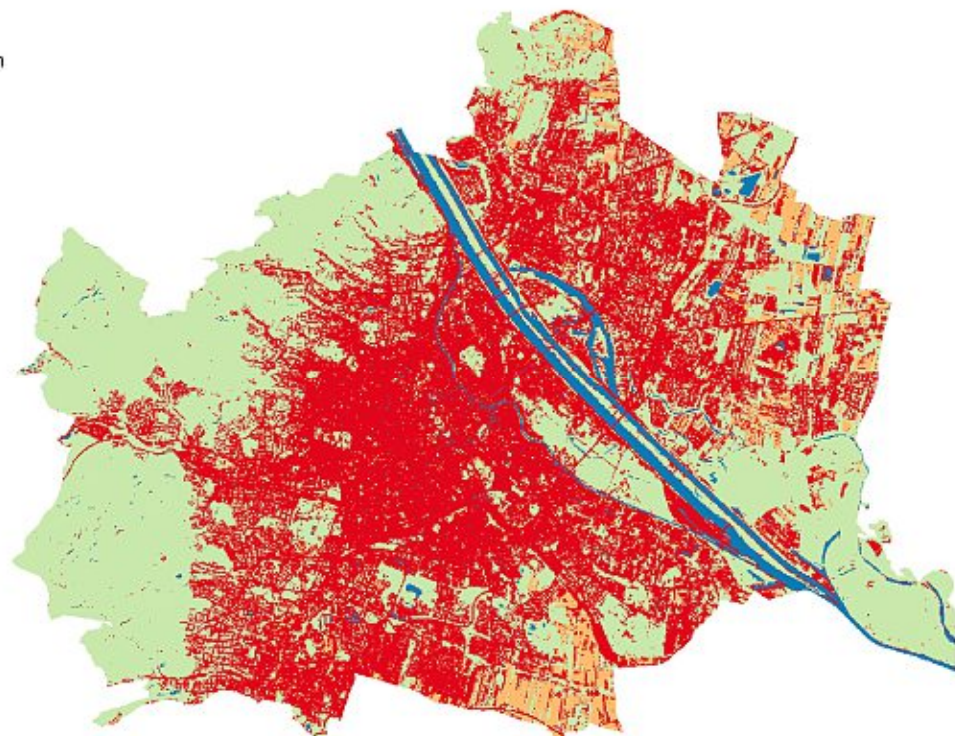
- Water
- Built-up
- Vegetation
- Bare soil



Land use/land cover classification

LULC classes (2020)

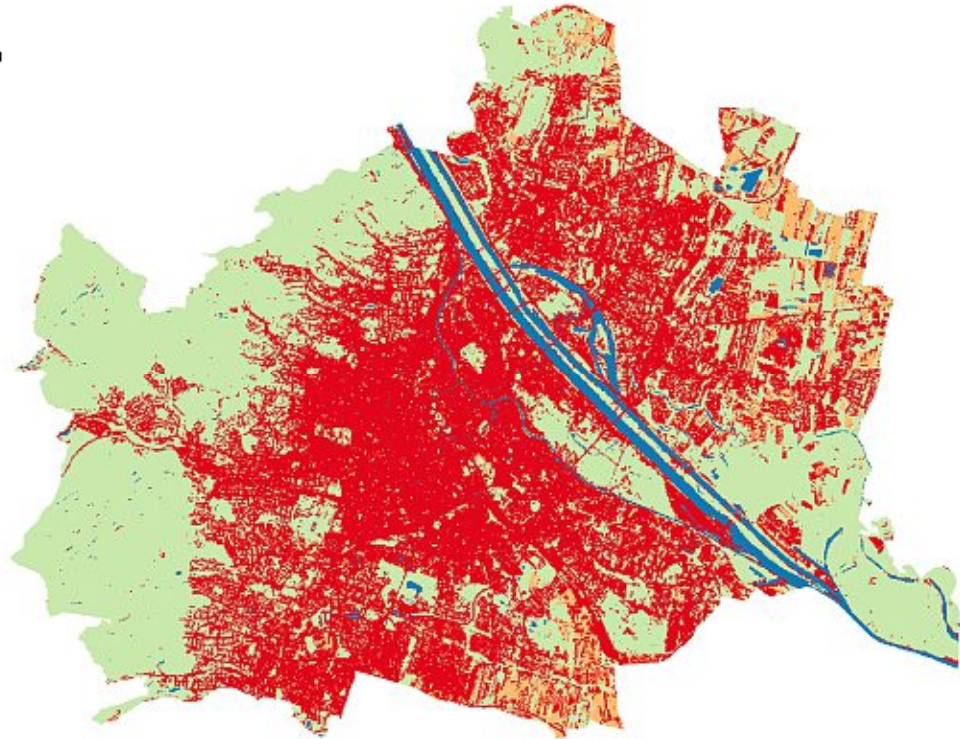
- Water
- Built-up
- Vegetation
- Bare soil



Land use/land cover classification

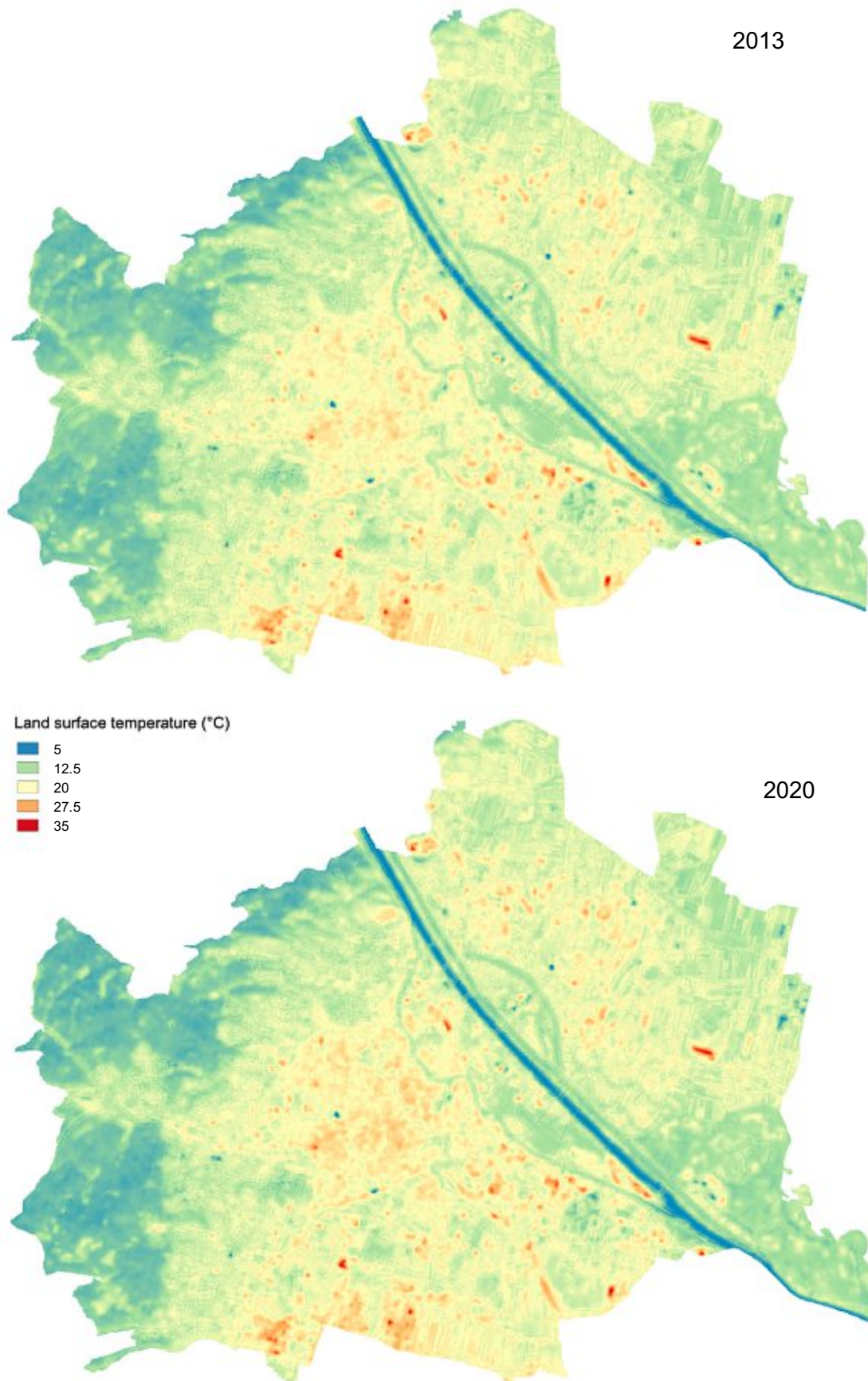
LULC classes (2055)

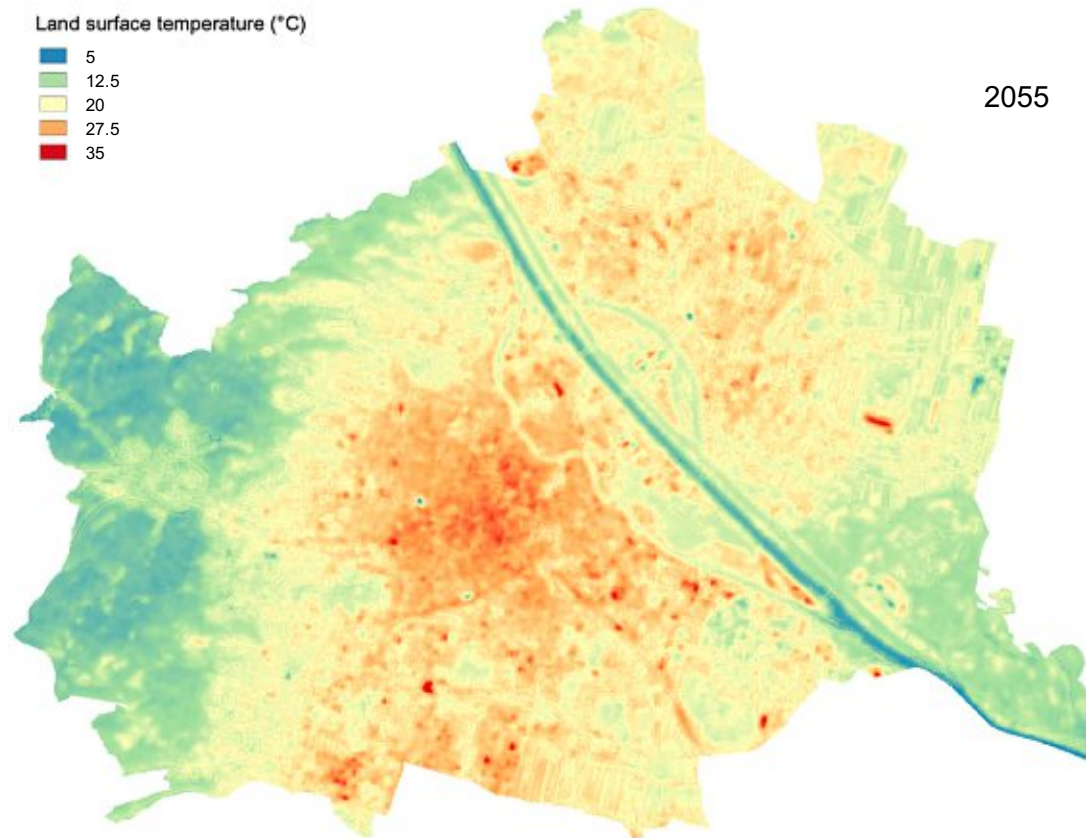
- Water
- Built-up
- Vegetation
- Bare soil



Appendix 3: LULC classifications (past, present, predicted) (QGIS 2020)

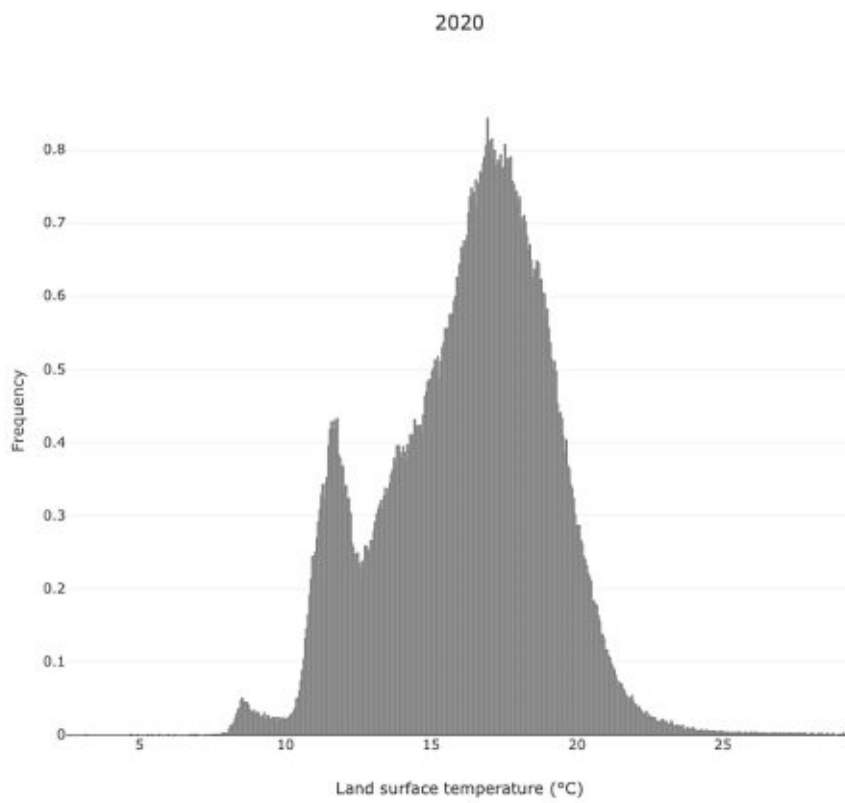
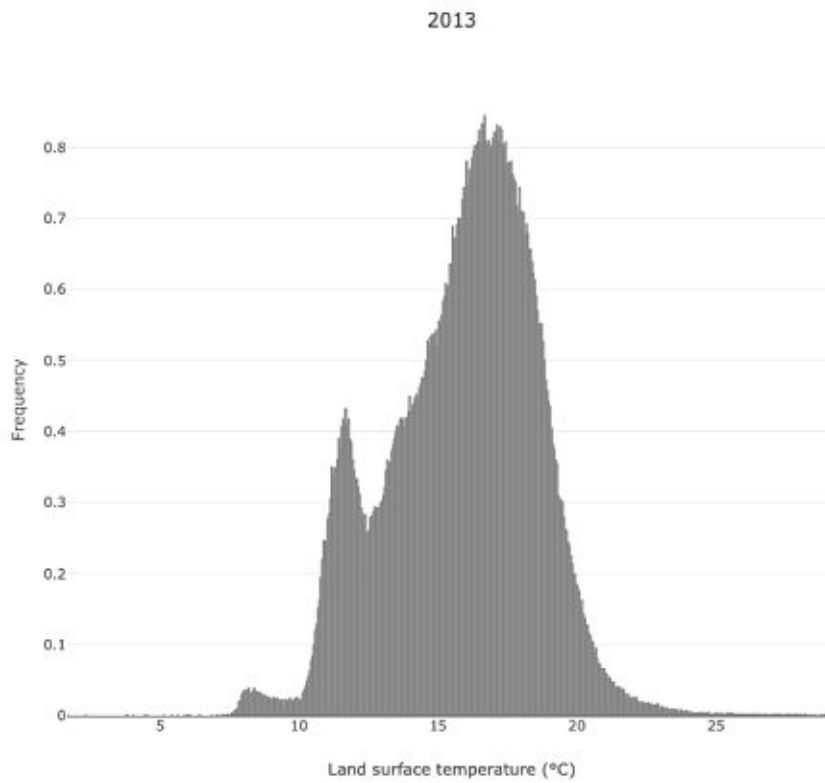
Appendix 4: Land surface temperature maps

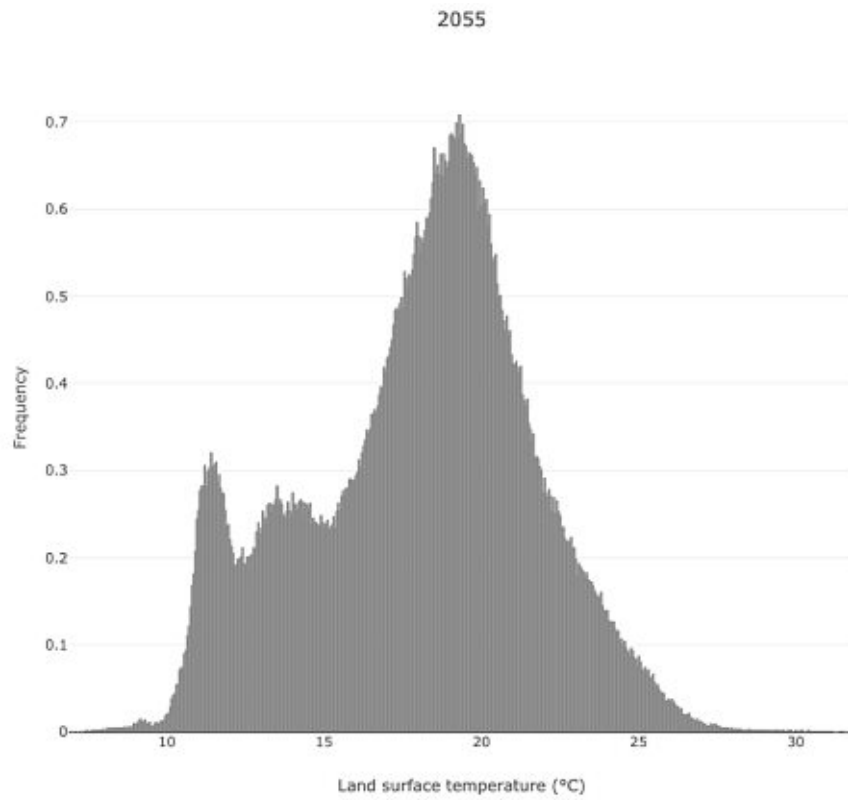




Appendix 4: Land surface temperature results (past, present, predicted) (QGIS 2020)

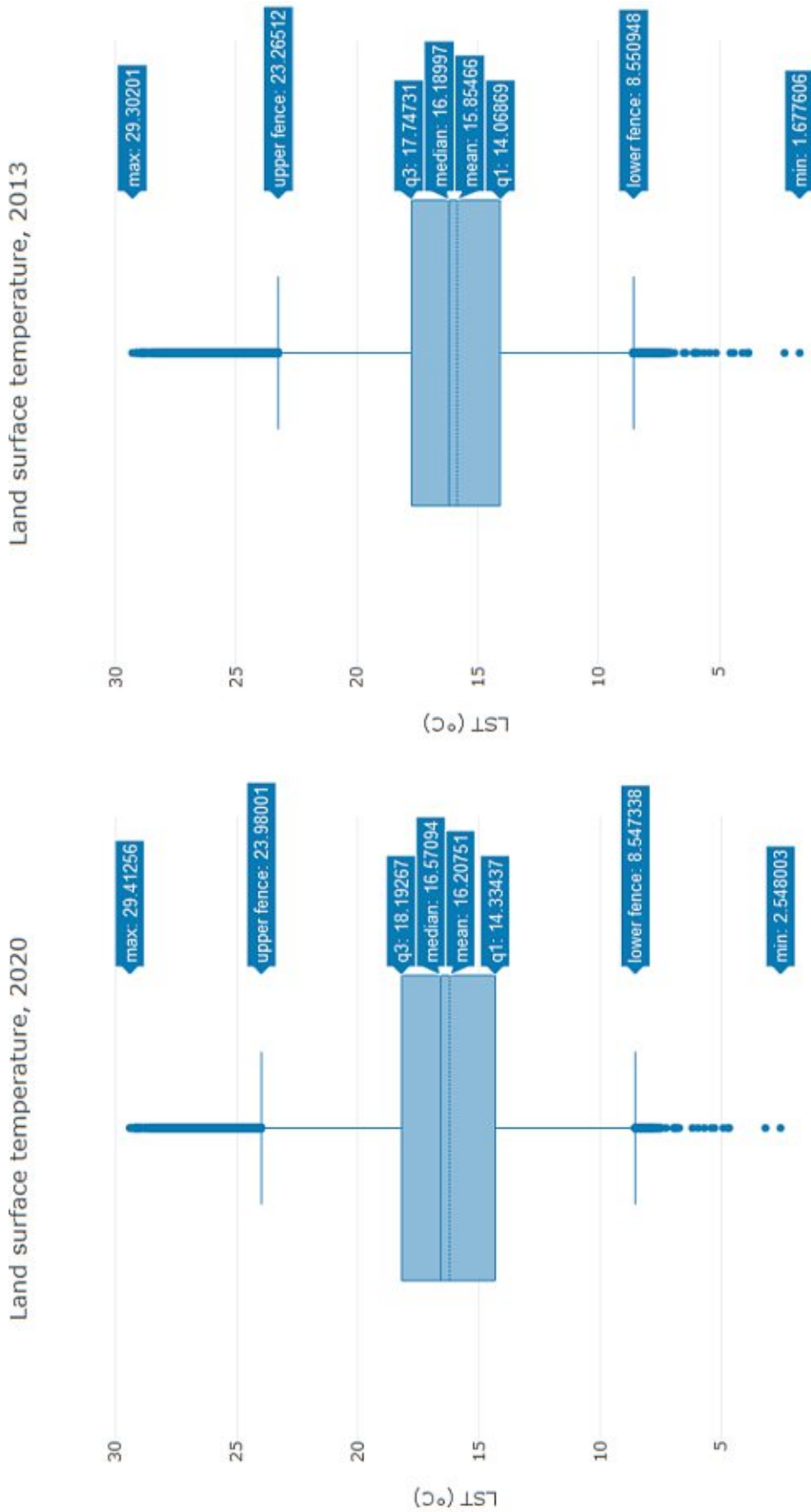
Appendix 5: Histograms of the land surface temperature calculations





Appendix 5: Histograms of the land surface temperature frequency in Vienna (x-axis: pixel value i.e. LST (°C), y-axis: frequency) (QGIS, 2020)

Appendix 6:



Appendix 6: Box plots of the LST outputs of 2013 and 2020 (QGIS 2021)